

1 **Investigating the role of typhoon-induced gravity waves and**
2 **stratospheric hydration in the formation of tropopause cirrus**
3 **clouds observed during the 2017 Asian monsoon**

4 Amit Kumar Pandit¹, Jean-Paul Vernier^{1,2}, Thomas Duncan Fairlie^{2†}, Kristopher M. Bedka²,
5 Melody A. Avery², Harish Gadhavi³, Madineni Venkat Ratnam⁴, Sanjeev Dwivedi⁵,
6 Kasimahanthi Amar Jyothi⁶, Frank G. Wienhold⁷, Holger Vömel⁸, Hongyu Liu^{1,2}, Bo Zhang^{1,2},
7 Buduru Suneel Kumar^{9*}, Tra Dinh¹⁰, and Achuthan Jayaraman¹¹

8 ¹National Institute of Aerospace, Hampton, USA

9 ²NASA Langley Research Center, Hampton, USA.

10 ³Physical Research Laboratory, Ahmedabad, India.

11 ⁴National Atmospheric Research Laboratory, Gadanki, India.

12 ⁵Meteorological Centre, India Meteorological Department, Ministry of Earth Sciences, Bhubaneswar, India.

13 ⁶National Centre for Medium Range Weather Forecasting, Noida, India.

14 ⁷ETH Zurich, Zurich, Switzerland.

15 ⁸National Centre for Atmospheric Research, Boulder, USA.

16 ⁹Tata Institute of Fundamental Research Balloon Facility, Hyderabad, India.

17 ¹⁰Department of Physics, University of Auckland, New Zealand.

18 ¹¹Bangalore University, Bangalore, India.

19 † Deceased on 27 April 2022

20 * Deceased on 12 February 2024

21 Correspondence to: Amit Kumar Pandit (amitkpandit86@gmail.com)

22
23 **Abstract.** We investigate the formation mechanism of a tropopause cirrus cloud layer observed during the Balloon
24 measurement campaigns of the Asian Tropopause Aerosol Layer (BATALL) over Hyderabad (17.47° N, 78.58° E),
25 India on 23 August 2017. Simultaneous measurements from a backscatter sonde and an optical particle counter
26 onboard a balloon flight revealed the presence of a subvisible cirrus cloud layer (optical thickness ~0.025) at the
27 cold-point tropopause (temperature ~ -86.4 °C, altitude ~17.9 km). Ice crystals in this layer are smaller than 50 µm
28 with a layer-mean ice-crystal number concentration of about 46.79 L⁻¹. Simultaneous backscatter and extinction
29 coefficient measurements allowed us to estimate range-resolved lidar ratio inside this layer with a layer-mean value
30 of about 32.18±6.73 sr which is in good agreement with earlier reported values at similar cirrus cloud temperatures.
31 The formation mechanism responsible for this tropopause cirrus is investigated using a combination of three-
32 dimensional back-trajectories, satellite observations, and ERA5 reanalysis data. Satellite observations revealed that
33 the overshooting convection associated with a category-3 typhoon *Hato*, which hit Macau and Hong Kong on 23
34 August 2017 injected ice into the lower stratosphere. This caused a hydration patch that followed the Asian Summer
35 Monsoon anticyclone to subsequently move towards Hyderabad. The presence of tropopause cirrus cloud layers in
36 the cold temperature anomalies and updrafts along the back-trajectories suggested the role of typhoon-induced
37 gravity waves in their formation. This case study highlights the role of typhoons in influencing the formation of
38 tropopause cirrus clouds through stratospheric hydration and gravity waves.

1 **1 Introduction**

2
3 Cirrus clouds are composed of non-spherical ice crystals that exhibit high variability in their size and
4 shapes. Optically thin cirrus coverage is highest over the tropics in a region between the top of maximum convective
5 outflow (near 12-14 km) and the cold-point tropopause (CPT, between 16 and 18 km) called the Tropical
6 Tropopause Layer (TTL; Randel and Jensen (2013)). Due to their frequent occurrence at high altitudes and cold
7 temperatures, and their thin-wispy structures, cirrus clouds trap long-wave terrestrial radiation more efficiently than
8 they reflect incoming short-wave solar radiation (Lohmann and Gasparini, 2017). Therefore, high thin cirrus clouds
9 induce a net warming impact on the climate system (Gasparini and Lohmann, 2016; Hong et al., 2016). The
10 radiative effects of cirrus clouds depend on their macrophysical (coverage, altitude, geometrical thickness) and
11 microphysical properties (number concentration, mass density and size and shape distributions of ice crystals) (Liou,
12 1986, 2005). Higher cirrus clouds have a larger warming effect on climate than those at lower levels (Lohmann and
13 Gasparini, 2017). Simulations using General Circulation Models (GCMs) have shown that the radiative impact of
14 cirrus clouds is sensitive to small changes in the number concentration of small ice crystals (Sanderson et al., 2008;
15 Mitchell et al., 2008). In this context, subvisible cirrus clouds (having optical thickness less than 0.03 at visible
16 wavelengths) occurring near the CPT are important because they are the highest type of cirrus clouds with
17 significant horizontal coverage. Subvisible cirrus clouds can have a relatively long lifetime because they usually
18 consist of low concentrations of small ice crystals, which are more slowly removed by sedimentation and yield
19 greater radiative heating than larger ones, given the same ice mass (Fu and Liou, 1993).

20 Apart from their radiative impact, subvisible cirrus clouds play an important role in regulating the water
21 vapour in the upper troposphere and lower stratosphere (UTLS) region through dehydration (Jensen et al., 1996).
22 Dehydration efficiency depends on microphysical processes such as nucleation, growth and sedimentation (Rollins
23 et al., 2016). Understanding of microphysical processes under different dynamical forcings and their representation
24 in GCMs remain poor due to numerous factors, one being the lack of accurate measurements of microphysical
25 properties of ice crystals with particle sizes less than 100 μm from the current generation probes (Heymsfield et al.,
26 2017; Baumgardner et al., 2017; Kuhn and Heymsfield, 2016). In situ measurements provide accurate information
27 about the microphysical properties, which are essential for estimating their radiative impact on climate and for the
28 calibration and validation of ice-cloud products from passive and active remote sensing sensors. Balloons and
29 aircrafts are the most common in situ measurement platforms for ice crystal microphysical properties. Due to their
30 slow ascent, balloons provide cloud vertical profiles at high resolution, unlike aircrafts which provide larger
31 horizontal coverage but miss fine vertical information and detailed imaging of ice crystal habits. Moreover, ice
32 measurements using balloons do not suffer as much from shattering effects and do not require corrections due to
33 compressed air as in case of aircraft measurements under its wings (Wolf et al., 2018).

34 There have been several in situ measurements of tropical cirrus clouds using balloon-borne and aircraft-
35 based instruments (Krämer et al., 2016; Jensen et al., 2017; Schoeberl et al., 2019; Krämer et al., 2020 and
36 references therein). However, most of those measurements were over Australia, Brazil, Central America, Europe,
37 and the Western Pacific. Only a limited number of field campaigns have occurred over the Asian Summer Monsoon

1 (ASM) region (Krämer et al., 2020), despite the important role played by ASM in the transport of aerosols (Vernier
2 et al., 2015, 2018), water vapour (Nützel et al., 2019; Khaykin et al., 2022; Wang et al., 2019) and the formation of
3 cirrus clouds (Ueyama et al., 2018) in the UTLS region. Additionally, the ASM region has the largest coverage of
4 high-altitude cirrus and sub-visible cirrus clouds during the boreal summer (Martins et al., 2011). Field campaigns
5 such as the Balloon measurement campaigns of the Asian Tropopause Aerosol Layer (BATAL) (Vernier et al.,
6 2018) and aircraft campaigns such as StratoClim (Krämer et al., 2020) and the Asian Monsoon Chemical and
7 Climate Impact Project (ACCLIP, https://www.eol.ucar.edu/field_projects/acclip) have been organized over the
8 ASM region to understand the physical, chemical, and dynamical characteristics of the Asian Tropopause Aerosol
9 Layer (ATAL) along with cirrus cloud microphysics.

10 Satellite measurements have shown that the UTLS aerosol optical depth between 13 and 18 km altitude
11 over the ASM region has increased three-fold since the late 1990s (Vernier et al., 2015). A balloon-borne study over
12 Tibetan Plateau (He et al., 2019) also showed evidence for the hygroscopic growth of particles inside the ATAL.
13 These may have significant impact on the microphysics of cirrus clouds, especially subvisible cirrus clouds that
14 occur in the proximity of CPT during the ASM (Vernier et al., 2018). In this context, long-term (1998-2013) lidar
15 observations over a tropical station Gadanki (13.5° N, 79.2° E) in south India have shown an increase in the fraction
16 of subvisible cirrus clouds (Pandit et al., 2015). Also, the StratoClim campaign measurements in July and August
17 2017 from Nepal have shown the presence of solid ammonium nitrate particles from surface ammonia sources
18 (Höpfner et al., 2019), which act as efficient ice-nuclei in the presence of ammonium sulphate particles as shown in
19 the cloud chamber experiments (Wagner et al., 2020). In general, anthropogenic activities are expected to influence
20 the occurrence and properties of cirrus clouds by meteorological, aerosol-induced or cloud-induced changes
21 (Kärcher, 2017). However, these changes over the ASM region, which is one of the most polluted regions of the
22 globe, are not well known and warrant further investigations.

23 The UTLS region during the ASM is dominated by the complex interplay among frequent deep convection,
24 gravity waves, and large-scale updrafts which directly and/or indirectly lead to the formation of cirrus clouds either
25 through liquid-origin clouds or through in situ freezing mechanisms (Krämer et al., 2016). These dynamical
26 processes directly influence the microphysical properties of cirrus clouds. For example, slow updraft leads to thinner
27 cirrus clouds with low IWC while faster updraft leads to thicker cirrus clouds with higher IWC (Krämer et al.,
28 2016). A study (Ueyama et al., 2018) done using a one-dimensional (vertical), time-dependent cloud microphysical
29 model, diabatic back-trajectories, and observations of convective clouds has suggested that nearly all the
30 enhancement of water vapour and clouds at 100 hPa level over the ASM are due to convective saturation with
31 minimum impact from the convectively detrained ice. This is in contrast to another recent study (Wang et al., 2019)
32 where convective lofting of ice during the ASM is found to be the most important source of water vapour at 100 hPa
33 level in the 10-40° N region. Khaykin et al. (2022) have recently shown evidence of direct convective hydration
34 (water vapour mixing ratio >10 ppmv) by the overshooting convection over the ASM region using StratoClim
35 aircraft measurements. Such large-scale organized convective systems in the southern ASM anticyclone are also
36 associated with synoptic-scale dehydration near the tropopause. In this context, the role of large-scale organized

1 deep convection over the East Coast of India in the formation of tropopause cirrus clouds is a subject of interest for
2 the BATAL campaigns organized in Hyderabad (17.47° N, 78.58° E), India (see Sect. 2.1).

3 In addition to meso-scale deep convection, overshooting convection frequently occurs in the tropical
4 cyclones (Roms and Kuang, 2009), especially during their intensification (Horinouchi et al., 2020). Tropical
5 cyclones (typhoons) during the ASM have also been seen to cause dehydration near the CPT (Li et al., 2020) and
6 hydration in the lower stratosphere (Jiang et al., 2020). Climate change is expected to strengthen and increase the
7 occurrence frequency of such typhoons (Stocker et al., 2013). Extreme tropical convection is expected to impact
8 TTL water vapour and cirrus clouds (Aumann et al., 2018). However, a recent climate model study (Smith et al.,
9 2022) suggests that the role of convective ice injection to the stratospheric water vapour budget will remain
10 constrained by large-scale temperatures in a warmer climate. ~~Thus, a change in large-scale temperature fields in the
11 TTL such as those created by tropical cyclones (Biondi et al., 2015) or intense convective systems (Biondi et al.,
12 2012) will determine how much injected ice will be converted into water vapour in addition to injection altitude and
13 frequency of convective penetration.~~ Thus, it is essential to understand how such systems influence the large-scale
14 temperature fields and hence cirrus cloud formation in the TTL. In this context, the ASM, which is influenced by
15 frequent deep convective systems and tropical cyclones, is preferred region for studying such influence on cirrus
16 clouds as presented here.

17 In the UTLS region, deep convection generates gravity waves which are known to influence the cold-point
18 tropopause temperature, cirrus cloud formation and hence cause dehydration in the UTLS region (Schoeberl et al.,
19 2015, 2016). Using radiosonde observations over the tropical Western Pacific region, Kim and Alexander (2015)
20 have shown that the CPT temperature is directly modulated by the vertically propagating waves irrespective of any
21 change in the mean upwelling. Later, Kim et al. (2016) showed ubiquitous influence of waves on the TTL cirrus
22 clouds using airborne observations of temperature and cirrus clouds obtained over the Western Pacific during the
23 ATTREX campaign. Several studies (Wu et al., 2015; Nolan and Zhang, 2017; Kim et al., 2009) have reported
24 anomalies in temperature and vertical wind speed associated with semi-circular gravity waves generated from the
25 typhoon centre propagating horizontally and vertically through the troposphere, stratosphere, and mesosphere in
26 expanding spirals with horizontal wavelengths typically in the range of 50-500 km and periods from 1 hour to 1.6
27 days.

28
29 This paper presents a case study of in situ measurements of microphysical and optical properties of a
30 tropopause cirrus cloud layer observed during the BATAL campaign using balloon-borne instruments (a backscatter
31 sonde and an optical particle counter) capable of detecting very thin cirrus clouds consisting of ice crystals smaller
32 than 100 μm . We also demonstrate the usefulness of combined measurements from these instruments in measuring
33 the range-resolved lidar ratio in situ for a tropical tropopause cirrus cloud layer for the first time (to the best of our
34 knowledge). Using back-trajectory calculations and their intersection with the convective clouds observed by
35 radiometers on the Himawari-8 geostationary satellite, we also investigate the origin of the air masses sampled
36 during the balloon flight. The formation mechanism and properties of tropopause cirrus clouds along the back-
37 trajectories are examined using the satellite observations. Section 2 describes the BATAL campaign, balloon-borne

1 instruments, satellite, and model data used in this study. Section 3 discusses the results and Sect. 4 contains the
2 summary.

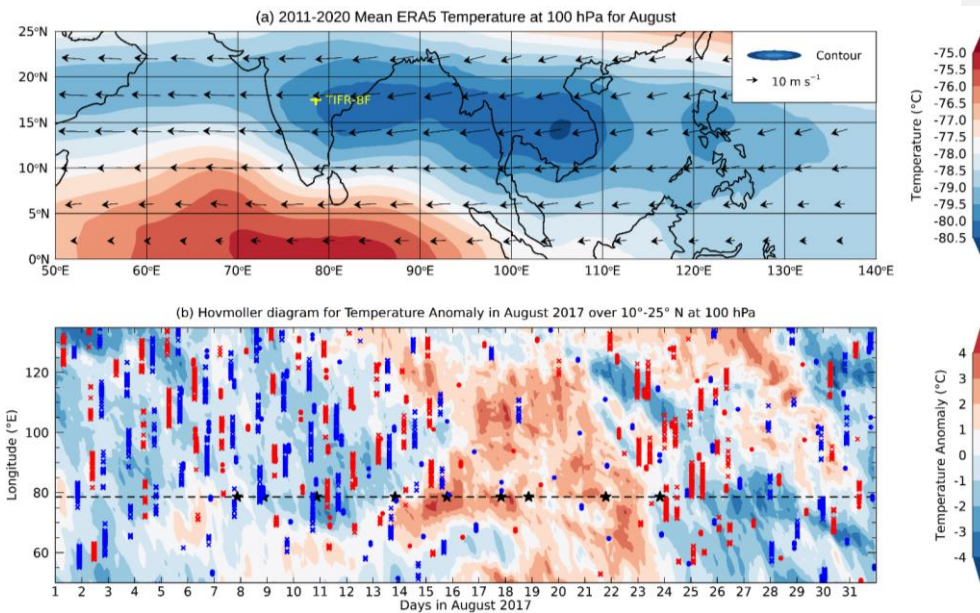
3

4 2 Data and method

5 2.1 BATAL campaign and general meteorological conditions

6

7 The balloon measurements were carried out under the framework of the India Space Research Organization
8 (ISRO)-National Aeronautics and Space Administration (NASA) joint project called BATAL (Vernier et al., 2018)
9 during August 2017 from Tata Institute of Fundamental Research Balloon Facility (TIFR-BF,
10 <https://www.tifr.res.in/~bf/>) located at 17.47° N, 78.58° E, in Hyderabad, India. During the ASM period (June to



11

12 **Figure 1:** (a) Filled colour contour showing the 10-year (2011-2020) mean ERA5 temperature superimposed
13 with wind vectors representing the mean ERA5 horizontal wind speed and direction at 100 hPa pressure level
14 for the month of August. The yellow “plus” sign indicates the location of the TIFR-BF in Hyderabad, India.
15 (b) Hovmöller plot for the anomaly in temperature from ERA5 temperature at 100 hPa pressure level for
16 August 2017. The anomaly is computed by subtracting the monthly mean (for August 2017) temperature for
17 each grid between 10° N and 25° N. The dashed horizontal black line marks the longitude (78.58° N) of the
18 TIFR-BF with each black star on it showing the launch time of the balloon. The red (blue) filled circles and
19 crosses superimposed on the filled colour contours represent the locations of cirrus cloud layers detected by
20 CALIOP and CATS during daytime (nighttime), respectively, with their base altitude located at 16 km or
21 above.

22 August), deep convective clouds developing over the Bay of Bengal (BoB) and over the land, especially over the
23 Indian East Coast, cause precipitation in the late afternoon and early evening hours. Climatologically, Hyderabad
24 receives highest rainfall during the months of July and August due to frequent deep convection. Launching a heavy

1 plastic balloon flight from TIFR-BF during this time is thus quite challenging due to strong south-westerly surface
2 winds and frequent precipitation. During this period, the Tropical Easterly Jet (TEJ) with maximum wind speeds of
3 about 40 m s^{-1} prevails over Hyderabad in the UTLS region (Vernier et al., 2018). TEJ brings moisture from the
4 Bay of Bengal, Western Pacific, and Southeast Asia (Das et al., 2011) necessary for cirrus cloud formation. Also,
5 the tropopause over Hyderabad is extremely cold (minimum temperature reaching about -86°C) as observed during
6 the BATAL campaigns (Vernier et al., 2018) as compared to north India. The 10-year (2011-2020) mean
7 temperature at 100 hPa pressure level ($\sim 16.5 \text{ km}$ altitude) from ERA5 (described in Sect. 2.4.3) during the month
8 of August shows a pool of cold-region (with temperature between -78°C and -80°C) between 10°N and 20°N
9 from the South China Sea to the Indian East Coast with Hyderabad located right at the edge (Fig. 1a). This cold
10 region, often influenced by deep convective activities and the TEJ, seems to be a hot spot for laminar cirrus clouds
11 as evident from the observations of two space-borne lidars (described in Sect. 2.3.1 and 2.3.2) as shown in Fig. 1(b)
12 for the month of August 2017. The occurrence of these cirrus clouds with their base altitude at or above 16 km is
13 associated with negative temperature anomaly estimated from the ERA5 temperature by subtracting the monthly
14 mean temperature from each grid ($0.25^\circ \times 0.25^\circ$) in this cold pool (Fig. 1b). All these factors make TIFR-BF an
15 ideal location for cirrus cloud studies during the ASM. A total of 9 balloon flights were launched from TIFR-BF
16 during August 2017 (Vernier et al., 2018) and the timings of these flights are shown in Fig. 1(b). The balloon-borne
17 instruments used for measuring the cloud properties are described in Sect. 2.2 below.

18

19 **2.2 Balloon-borne observations**

20

21 On the night (at 20:03 UTC or 01:33 LT) of 23 August 2017, balloon-borne instruments onboard a Heavy Flight
22 (HF; see Vernier et al. (2018) for description) were launched from TIFR-BF to measure the vertical distribution of
23 aerosols, clouds and meteorological parameters as described in the sub-sections below. Satellite and model data
24 have also been used in this study to support the balloon observations, which are described in the following sub-
25 sections.

26

27 **2.2.1 Compact Optical Backscatter Aerosol Detector (COBALD)**

28 COBALD is a unique lightweight (about 500 g) balloon-borne backscatter sonde developed at the Institute of
29 Atmospheric and Climate Science, Swiss Federal Institute of Technology (ETH), Zurich. COBALD enables us to
30 detect optically thin layers of aerosols and clouds at high vertical resolution (Brabec et al., 2012; Cirisan et al.,
31 2014; Martínez et al., 2021; Vernier et al., 2015, 2016, 2018; Brunamonti et al., 2018). Additional details on
32 COBALD is presented in Appendix A. COBALD gives backscatter ratio (BSR) at two wavelengths (455 nm and
33 940 nm) which is an optical analogue for particle mixing ratio. (COBALD consists of two high power (500 mW)
34 Light Emitting Diodes (LEDs) which emit light at 455 nm (blue) and 940 nm (near-infrared) wavelengths. A
35 silicon photodiode placed between the two LEDs collects the light backscattered from the air borne particles
36 (molecules, aerosols, and clouds). When connected with an iMet radiosonde, the instrument adds backscatter and
37 monitor signals at both wavelengths to the radiosonde pressure, temperature, relative humidity, wind speed and
38 wind direction data at a rate of 1 Hz to the receiving ground station. The concurrent profiles of pressure,

1 temperature and backscattered counts are used to calculate backscatter ratio (BSR), the ratio of total (molecules and
2 particulate) backscatter coefficient ($\beta = \beta_p + \beta_m$) to the molecular backscatter coefficient (β_m) at a given wavelength.
3 The BSR is calibrated in a region of the atmosphere minimally affected by aerosols and adjusted with a reference
4 density signal derived from pressure and temperature. The absolute error associated with BSR is within 5 % while
5 its precision is better than 1 % in the UTLS region (Vernier et al., 2015). The BSR is an optical analogue for
6 particle mixing ratio. The ratio of $(BSR_{940}-1)$ at 940 nm to $(BSR_{455}-1)$ at 455 nm, defined as the colour index (CI),
7 gives qualitative information about particle size (Cirisan et al., 2014; Vernier et al., 2015). On substituting the
8 molecular backscatter coefficient at 455 nm and 940 nm wavelengths, CI reduces to

$$9 \quad CI = 18 \times \left(\frac{\beta_{p940}}{\beta_{p455}} \right) = 18 \times CR \quad (1)$$

10 where β_{p455} and β_{p940} are particulate backscatter coefficients at 455 nm and 940 nm, respectively and the ratio $\frac{\beta_{p940}}{\beta_{p455}}$
11 is called the particulate colour ratio (CR). CR value near unity indicates the presence of cloud layer whereas values
12 below 0.7 indicates aerosol presence (Vernier et al., 2015; Brunamonti et al., 2018). Ångström's exponent
13 estimated from the BSR_{940} and BSR_{455} is used to estimate the backscatter ratio at 532 nm (BSR_{532}) following
14 Vernier et al. (2015). After applying the Field of View (FOV) corrections to COBALD backscatter coefficient as
15 suggested by Brunamonti et al. (2021), an extinction coefficient profile is obtained at 532 nm wavelength by using
16 the BSR_{532} profile and assuming a constant lidar ratio for cirrus clouds following the CALIOP L2 V4 algorithm
17 where initial lidar ratio is a sigmoid function of centroid temperature ± 10 sr (Young et al., 2018). By integrating
18 these extinction coefficients between the base and top altitudes of the cloud layer, optical thickness (τ) of the cloud
19 layer is estimated. The extinction coefficient derived from the COBALD is used for estimating the IWC of the
20 tropopause cirrus cloud layer using a temperature-dependent parametrized relation derived from the aircraft
21 measurements (Heysmsfield et al., 2014) as described in the next sub-section (2.2.2).
22

23 2.2.2 SOLAIR Boulder Counter and the estimation of cloud microphysical properties

24 2.2.2.1 SOLAIR Boulder Counter

25
26 The Solair Boulder Counter is a medium-weight (~6 kg) portable, forward scattering-based particle counter from
27 Lighthouse Worldwide Solutions, USA ([https://www.golighthouse.com/en/airborne-particle-counters/boulder-](https://www.golighthouse.com/en/airborne-particle-counters/boulder-counter)
28 [counter](https://www.golighthouse.com/en/airborne-particle-counters/boulder-counter)), which uses an extreme life laser diode at 680 nm as a light source. Particles are sampled at a high flow
29 rate of 28.3 Litres per minute (LPM) and are directed to the laser beam. The light scattered at 45° angles from the
30 particles is collected and focused by collection optics onto a photo diode which converts it into electric pulses. The
31 pulse amplitude is a measure of particle size. The number of pulses as a function of pulse height gives particle
32 counts and size information. Particles are counted in six size channels between $5 \mu\text{m}$ and $100 \mu\text{m}$ viz., 5, 10, 25,
33 40, 50 and $100 \mu\text{m}$ with 50 % counting efficiency at $5 \mu\text{m}$ size and 100 % at other size bins. The Boulder Counter's
34 ability to measure large particles allows us to infer the distribution of larger air-borne particles such as cloud
35 droplets and ice crystals from a balloon platform. Particle counts in each bin are recorded onboard every 5 seconds
36 which when divided by the instantaneous sample flow gives particle number concentration for that size bin at that
37 time. Boulder Counter measurements were synchronized with COBALD measurements. The flow is controlled and

Formatted: Font: (Default) Times New Roman, 10 pt, Bold, Not Italic, Font color: Auto

Formatted: Border: (No border)

Formatted: Heading 4

1 monitored through an external mass-flow controller system. During the flight, the sample flow decreased gradually
 2 with decreasing pressure, but it remained above 10 LPM up to 20 km altitude. The entire system was adapted for
 3 balloon measurements and enclosed in a foam box to maintain the operating range of conditions during the balloon
 4 flight between 10 °C and 40 °C of temperature. The system was calibrated at the company before the flight and the
 5 performance of this system was also tested in a thermo-vacuum chamber prior to the balloon flight. To the best of
 6 our knowledge, this system is used for the first time for measuring ice particles in ice clouds from a balloon
 7 platform.

8 **2.2.2.2 Estimation of cloud microphysical properties**

11 Only data during the ascent flight are used for estimating the optical and microphysical properties of cirrus
 12 clouds. To estimate the microphysical (particle number concentration, effective diameter, and IWC) and the optical
 13 properties (extinction coefficient and lidar ratio) from the Boulder Counter data, a log-normal size distribution
 14 function was fit to the cumulative particle number concentration within the cloud layer. A single mode lognormal
 15 size distribution function is expressed as

$$16 \frac{d}{dr} N(r) = N_0 \frac{\exp\left[-\frac{1}{2} \left(\frac{\ln^2\left(\frac{r}{r_m}\right)}{\ln^2\sigma}\right)\right]}{r \ln\sigma \sqrt{2\pi}} \quad (2)$$

17 where N is the number concentration, N_0 is the total particle concentration in the mode, r is the radius, r_m is the
 18 median radius, and σ is the width of the distribution (Thomason and Peter, 2006). A previous study (Kuhn and
 19 Heymsfield, 2016) has shown that a log-normal distribution provides better match with the data in contrast to a
 20 gamma distribution. The first and the third moments of the size distribution are calculated from equation (2) which
 21 are then used to estimate the effective diameter (D_e) and IWC, respectively (described below).

22 The effective diameter of ice crystals is an important microphysical parameter used for the radiative
 23 calculations of ice clouds. It is defined as the ratio of absorption to the extinction cross-section of the ice crystals
 24 (Foot, 1988). Approximating ice crystals as spheres, D_e can be estimated using a log-normal particle size
 25 distribution from equation (3) as shown below:

$$26 D_e = 2 \frac{\int_0^r r^3 N(r) dr}{\int_0^r r^2 N(r) dr} \quad (3)$$

27 where the numerator and the denominator are the third and second moments of the particle size distribution
 28 function, respectively. We also estimated the effective diameter using its temperature dependence relation given by
 29 Heymsfield et al. (2014) as shown below in equation (4) to compare with that derived from the size distribution.

$$31 D_e = \alpha e^{\beta T} \quad (4)$$

32 where T is the temperature,

$$33 \alpha = 308.4, \beta = 0.0152 \text{ for } -56^\circ\text{C} < T < 0^\circ\text{C}.$$

$$34 \alpha = 9.1744 \times 10^4, \beta = 0.177 \text{ for } -71^\circ\text{C} < T < -56^\circ\text{C}.$$

$$35 \alpha = 83.3, \beta = 0.0184 \text{ for } -85^\circ\text{C} < T < -71^\circ\text{C}.$$

Formatted: Font color: Auto

Formatted: Font: (Default) Times New Roman, 10 pt, Bold, Not Italic, Font color: Auto

Formatted: Border: : (No border)

Formatted: Normal, Left, Indent: Left: 0", First line: 0", Line spacing: single

1
 2 Using the Airborne Tropical Tropopause Experiment (ATTREX) campaign data, Thornberry et al. (2017) have
 3 found that the effective diameter decreases more sharply at temperatures (T) below -81 °C (192 K) than previously
 4 found by Heymsfield et al. (2014). This decrease in median effective diameter for T<192 K is expressed as

$$5 \quad D_e = 12 + 28e^{0.625(T-192)} \quad (5)$$

6
 7
 8 We also estimated the extinction coefficient from our particle size distribution measurements, using a geometric
 9 optical approximation which assumes that the extinction coefficient is two times the total cross-sectional area of the
 10 ice crystals. Assuming that the ice particles are close to being spherical, we use the equation for extinction
 11 expressed in Thornberry et al. (2017):

$$12 \quad \sigma_{ext} = 2 \times \sum_j N_j \pi r_j^2 \quad (6)$$

13 where N_j is the ice particle number concentration (in L^{-1}) corresponding to the particle radius r_j (in μm) with j
 14 ranging from 1 μm to 25 μm . The ratio of σ_{ext} (from equation 6) to the particulate backscatter coefficient (β_p)
 15 obtained from COBALD gives lidar ratio (discussed in Sect. 3.3.4). [More details on the lidar ratio are presented in](#)
 16 [Appendix A.](#)

17 IWC is an important microphysical parameter for estimating the radiative impact of cirrus clouds as well as for
 18 understanding the microphysical and dynamical processes occurring within them (Heymsfield et al., 2017). We
 19 estimated IWC for the tropopause cirrus independently from the COBALD backscatter and the Boulder Counter
 20 measurements. IWC was obtained from COBALD data using the extinction coefficient (σ_{ext}) and the effective
 21 diameter (D_e) estimated from the Equation 9 (e) given in Heymsfield et al. (2014) as shown below.

$$22 \quad IWC = \sigma_{ext} \left(\frac{0.91}{3} \right) D_e \quad (7)$$

23 Here, D_e is obtained from equation (4) using temperature measurements. Using the ATTREX in situ measurements,
 24 Thornberry et al. (2017) have given a new parameterization relation for the estimation of IWC from extinction
 25 coefficient in the temperature (T) range between 185 K (-88 °C) and 192 K (-81 °C) as shown below.

$$26 \quad IWC = \frac{0.92}{3} \sigma_{ext} (12 + 28e^{0.65(T-192)}) \quad (8)$$

27
 28 [IWC is estimated by multiplying the ice-density \(917 kg m⁻³\) with the total volume obtained from the third](#)
 29 [moment of the particle size distribution. ~~when multiplied with the ice density \(917 kg m⁻³\), it gives IWC.~~](#) IWC for
 30 the tropopause cirrus cloud layer derived from these abovementioned methods are compared in Sect. 3.3.5.

31 32 **2.2.3 India Meteorological Department (IMD) radiosonde profiles from the University of Wyoming**

33 We use daily (00 UTC) radiosonde profiles of meteorological parameters over the Meteorological centre,
 34 Hyderabad airport (17.45° N, 78.46° E) and its surrounding IMD stations such as Machilipatnam (16.2° N, 81.15°
 35 E), Visakhapatnam (17.7° N, 83.3° E), and Jagdalpur (19.08° N, 82.02° E), obtained from the University of

1 Wyoming Atmospheric Soundings website (<http://weather.uwyo.edu/upperair/sounding.html>). Only profiles during
2 the month of August 2017 are used in this study from these stations. The monthly mean temperature and wind
3 profiles are constructed by using 27 days of available data over Hyderabad during August 2017. The monthly mean
4 temperature and wind profiles are used to obtain anomalies from the profiles obtained on 23rd August 2017. In
5 order to obtain gravity-wave characteristics, profiles of zonal and meridional wind speed anomalies are used to
6 perform hodograph analysis by following a method described in (Leena et al., (2012). The results of hodograph
7 analysis are presented in Section 3.4.3 and in the supplementary information.

Formatted: Superscript

8 2.3 Satellite observations

9 2.3.1 Cloud Aerosol Lidar with Orthogonal Polarization (CALIOP)

10 CALIOP was a dual wavelength (532 and 1064 nm), dual-polarization, three channel space-borne lidar onboard the
11 Cloud-Aerosol Lidar and Infrared Pathfinder Satellite Observations (CALIPSO) orbiting around the Earth in a sun-
12 synchronous polar orbit at an altitude of about 705 km and an inclination of about 98.2° (Winker et al., 2009). It
13 has provided optical properties of aerosols and clouds distributed vertically in the Earth's atmosphere for 17 years
14 since June 2006 at unprecedented spatial resolution with a repeat cycle of 16 days at a given location. CALIOP can
15 detect thin and subvisible cirrus clouds (Martins et al., 2011) by measuring the attenuated backscatter coefficients
16 (at two wavelengths and two polarizations), followed by the retrieval of 532 nm extinction coefficients (Young et
17 al., 2018). IWC and effective diameter are estimated from these retrieved extinction coefficients, using a
18 temperature-dependent empirical fit derived from aircraft data (Heymsfield et al., 2014). In this study, we use
19 CALIOP Level 2 version 4.2 cloud profile (CPro) and cloud layer (CLay) data products having a horizontal
20 resolution of 5 km along the orbit track and 60 m vertical resolution between 8.2 and 20 km altitude range. We
21 obtained scattering ratio profiles from the total backscattering coefficient profiles at 532 nm wavelength and
22 molecular density profiles provided in the CPro data using method described in CALIOP Algorithm Theoretical
23 Basis Document (ATBD, Young et al., 2008).

26 2.3.2 Cloud-Aerosol Transport System (CATS) lidar

27 CATS was a three wavelength (355 nm, 532 nm and 1064 nm), dual polarization space-borne lidar intended to
28 provide vertical distribution of aerosols and clouds from the International Space Station (ISS) platform (Yorks et
29 al., 2014). It was launched in January 2015, operated until October 2017, and provided 33 months of aerosol and
30 cloud data. The orbit of ISS has an inclination of 51° and an altitude of about 405 km. This geometry provided
31 more coverage over the tropics and mid-latitudes when compared to CALIPSO with a shorter repeat cycle of 3
32 days and observations at various local times. In this study, we use 5 km horizontally averaged M7.2 Level 2,
33 Version 3.0 Operational Layer (OL) and Profile (OP) products. These products are obtained from one of the two
34 operational modes (M7.2) of CATS in which backscatter coefficient and depolarization ratio at 1064 nm are
35 measured. The horizontal and vertical resolutions are same as CALIOP data. We obtained scattering ratio from the
36 backscattering coefficient measurements at 1064 nm wavelength and molecular density profiles provided in the
37 data using method provided in CATS ATBD (Yorks et al., 2015).

1
2 **2.3.3 Cloud top height from Himawari-8 brightness temperature**
3

4 Himawari-8 is a geostationary satellite launched by Japan Meteorological Agency in October 2014 to observe
5 weather phenomena in 16 spectral bands (visible, near-infrared and infrared) at high resolution (Bessho et al.,
6 2016). Cloud-top temperature observations from 10.4 μm channel of the Himawari-8 satellite at an interval of 10
7 minutes have been used as proxy for convection. Low cloud-top temperature indicates the presence of deep
8 convective clouds and anvils. The horizontal resolution of cloud-top temperature is ~ 2 km at satellite nadir for the
9 infrared bands. The influence of deep convection on the tropopause cirrus clouds sampled by our balloon is
10 investigated by using a technique combining back-trajectory analysis (described in Sect. 2.4.1) and cloud-top
11 brightness temperature observations at 10.4 μm from the Himawari-8 developed by Bedka and Khlopenkov (2016).
12 This technique has been used earlier in Vernier et al., (2018) for studying the impact of deep convection including
13 overshooting convection on the air parcels sampled by the balloons.
14

15 **2.3.4 Humidity measurements from Aura-Microwave Limb Sounder (MLS)**
16

17 Level 2 Version 4.2 relative humidity with respect to ice (RHi) and water vapour mixing ratio (WVMR) data
18 products (Lambert et al., 2015) from the Microwave Limb Sounder (MLS) instrument onboard NASA's Aura
19 satellite are used. These data products are available at 55 pressure levels between 1000 and 10^{-5} hPa. The vertical
20 resolution of MLS-RHi range from 3.7 to 4.6 km between 68 and 100 hPa with an accuracy from 20 to 25 %. The
21 vertical resolution of MLS H₂O product is ~ 3 km with an accuracy of 8-9 % between 68 and 100 hPa levels.
22 Horizontal resolution along the orbit track is between 190 and 198 km over these pressure levels. The data
23 screening criteria specified for RHi and H₂O data by Livesey et al. (2017) have been applied to filter out the effect
24 of clouds.
25

26 **2.3.5 Temperature profiles from Global Navigation Satellite System Radio Occultation (GNSS-RO)**
27

28 High-resolution Global Navigation Satellite System Radio Occultation (GNSS-RO) dry temperature profile product
29 (Level 2, atmPrf) obtained from COSMIC-1, Metop A/B, GRACE, KOMPSAT-5, TSX, and TDX missions are
30 used to find the temperature near the tropopause cirrus clouds detected by CALIOP and CATS. These data are
31 provided by COSMIC Data Analysis and Archive Center (CDAAC, [https://cdaac-
33 www.cosmic.ucar.edu/cdaac/products.html](https://cdaac-
32 www.cosmic.ucar.edu/cdaac/products.html)) at 100 m altitude grids from 0 to 40 km altitude. Comparison of
34 GNSS-RO temperature profiles with those from radiosonde has shown good agreement (Anthes et al., 2008).
35 GNSS-RO data set have found many applications in the atmospheric science research such as in the study of the
36 gravity waves (Liou et al., 2003), thermal structure of the tropical cyclones (Biondi et al., 2013, 2015; Ravindra
37 Babu et al., 2015), volcanic cloud detection (Biondi et al., 2017), stratospheric thermal perturbation after
38 2019/2020 Australian pyroCb event (Khaykin et al., 2020) and tropopause cold-anomalies during the 2015 El Nino
39 event over the Pacific ocean (Ravindrababu et al., 2019).

1 **2.4 Model simulations and reanalysis data**

2 **2.4.1 NASA Langley Trajectory Model (LaTM) simulations**

3 The influence of deep convection on the tropopause cirrus cloud is investigated by using a combination of back-
4 trajectory analysis and cloud-top temperature observations from the Himawari-8 geostationary satellite (described
5 in Sect. 2.3.3). Meteorological fields from the NASA Global Modelling and Assimilation Office (GMAO) Goddard
6 Earth Observing System, Version 5.2 Forward Processing (GEOS-5.2 FP; Lucchesi et al., 2017) reanalysis are
7 used to compute three-dimensional back-trajectories using the NASA Langley Trajectory Model (Fairlie et al.,
8 2009, 2014). Back-trajectories from the location of the balloon measurement are run at every 100 m vertical
9 resolution. Temperature and wind speeds along the back-trajectories have also been obtained and used in this study
10 to understand the cloud-formation in the air-masses.

11 **2.4.2 NOAA HYSPLIT trajectories**

12 We used National Oceanic and Atmospheric Administration (NOAA) Hybrid Single-Particle Lagrangian Integrated
13 Trajectory (HYSPLIT) model (<https://www.ready.noaa.gov/HYSPLIT.php>) to compute forward trajectories of the
14 air parcels from the cirrus cloud altitudes measured from our balloon payload.
15
16

17 **2.4.3 ERA5 reanalysis data temperature, relative humidity, and cloud fraction**

18 We use hourly gridded (0.25° × 0.25°) temperature, relative humidity, and wind speed and cloud fraction from the
19 ERA5 data product available at 37 pressure levels to understand the spatio-temporal variation of the meteorological
20 variables and to supplement the satellite observations. ERA5 is the fifth generation of ECMWF reanalysis data
21 product, which provides improved representations of the troposphere and tropical cyclones at high spatial and
22 temporal resolution than its predecessor ERA-interim (Hersbach et al., 2020). With reference to the high-resolution
23 GNNS-RO temperature profiles, ERA5 temperature data provide most realistic tropopause temperatures compared
24 to other reanalyses (Tegtmeier et al., 2020). We derive the WVMR using the ERA5 temperature and relative
25 humidity data. The ice saturation vapour pressure is obtained from the relation given by Murphy and Koop (2005).
26 Over the ASM region, the WVMR obtained from ERA5 data provide a good representation of its vertical
27 distribution and variation between 60 and 100 hPa pressure levels with an average overestimation by 0.7-0.9 ppmv
28 (15-17 %) compared to that observed by Cryogenic Frost-point Hygrometer (CFH) during the ASM (Brunamonti et
29 al., 2019).

30 We list different sources of data and key parameters obtained from different instruments as discussed above in
31 Table 1.

32 **Table 1: List of different data sources and key parameters used in this study.**

S. No.	Instrument/model/reanalysis data	Key parameters
Balloon-borne measurements		
1.	COBALD	Backscatter ratios at 455 nm and 940 nm and colour ratio.
2.	iMet-1 radiosonde	Temperature (T), RH, u and v winds, GPS co-ordinates and

Formatted: Font: 10 pt

Formatted: Font: 10 pt

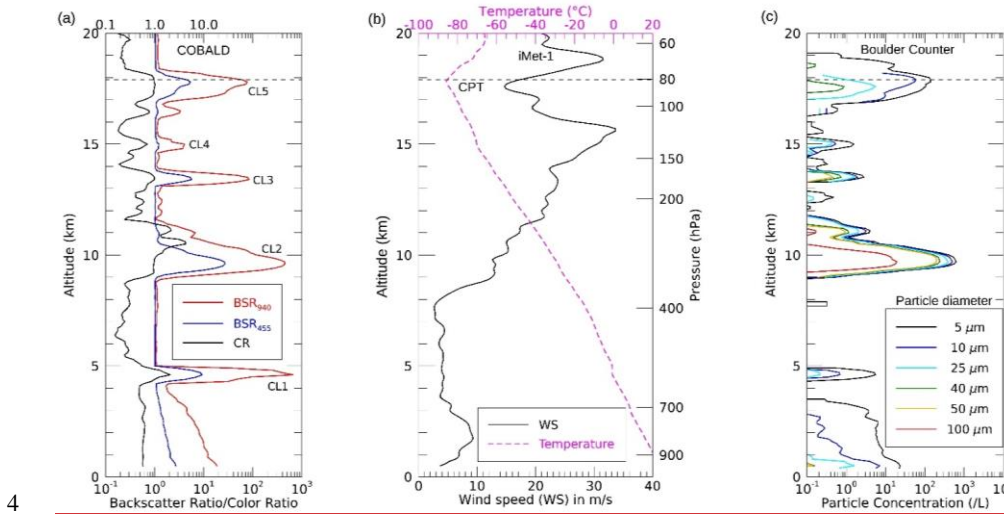
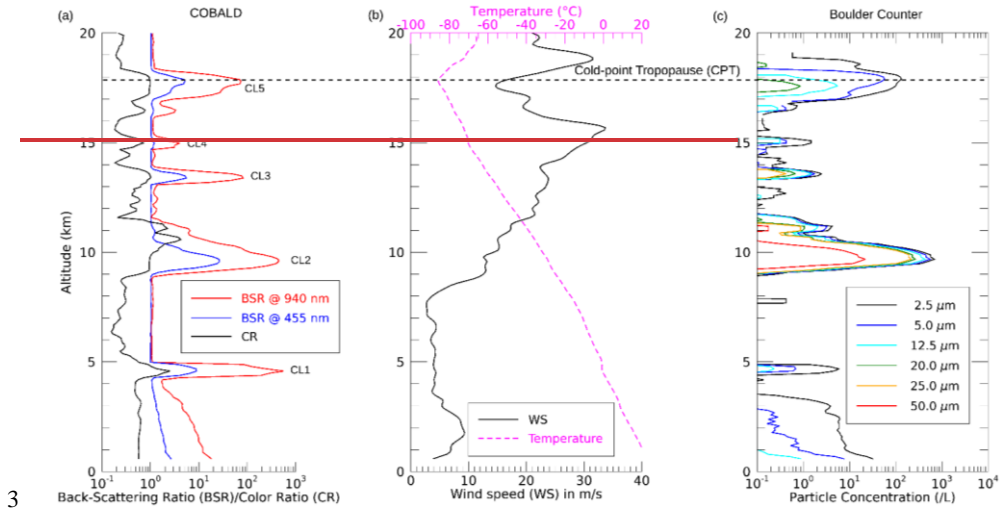
Formatted: Font: 10 pt

Formatted: Font: 10 pt

Formatted Table

Formatted: Font: 10 pt

1 well as ice crystals (Korolev et al., 2017). However, its cloud top is colder than -40°C indicating the presence of ice
 2 crystals which are smaller than $40\ \mu\text{m}$. These ice crystals have likely grown larger at the expense



5
 6 **Figure 2: Vertical profile of (a) backscatter ratio at 455 nm (blue line), 940 nm (red line) and colour ratio**
 7 **from radiosonde with horizontal dashed black line showing the CPT and (c) cumulative particle number**
 8

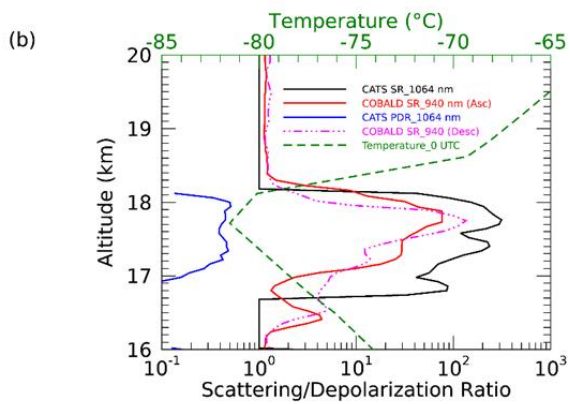
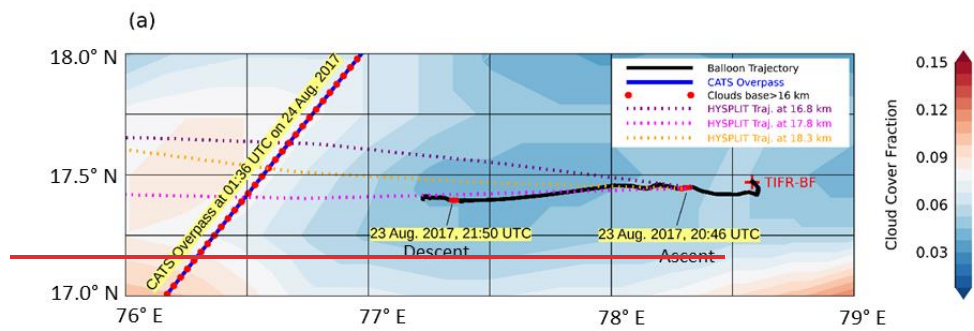
Formatted: Font: 12 pt
 Formatted: Normal (Web), Left, Indent: First line: 0",
 Space Before: 0 pt, Line spacing: single

1 concentration for particles having **diameterradius** greater than **2.5** (black line), **510** (blue line), **2512.5** (cyan
2 line), **420** (green line), **250** (yellow line) and **1050** μm (red line) obtained from the Boulder Counter
3 measurements on 23 August 2017 over Hyderabad, India during BATAL campaign. The vertical resolution is
4 **100 m** for each profile.

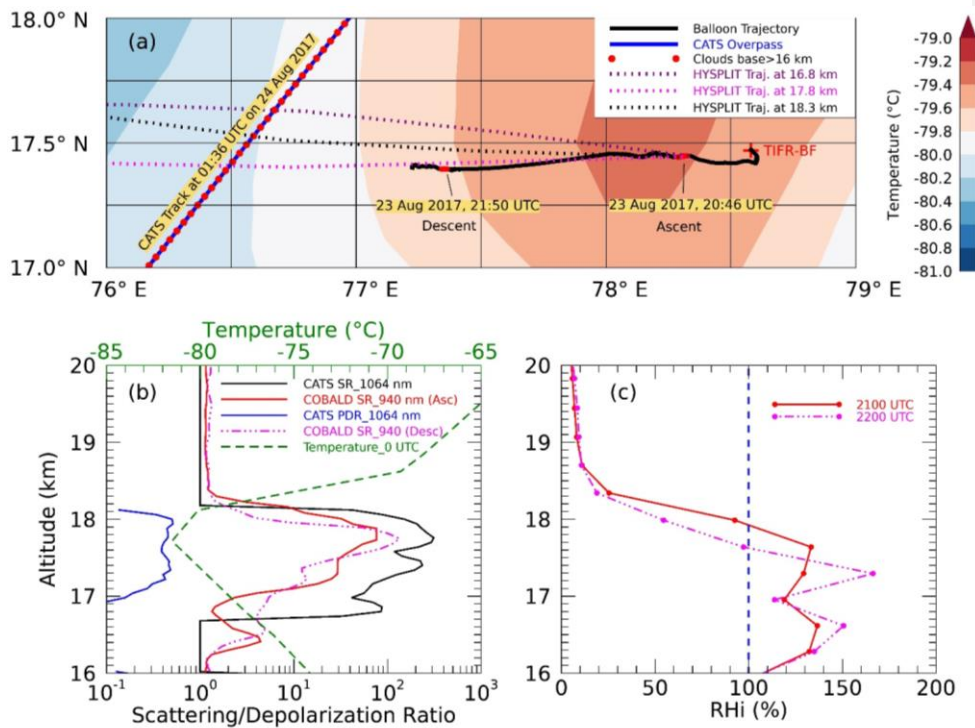
5 of ambient supersaturation and consequently have undergone sedimentation, as evidenced from the increased
6 concentration of larger sized (>40 , 50 and 100 μm) ice crystals a few hundred meters below the cloud top and near
7 the cloud base (Fig. 2c). The peak in BSR_{940} almost coincides with the peaks of particle concentration corresponding
8 to each size bins. The peak particle concentration (for diameter $> 5 \mu\text{m}$) in CL2 is found to be about 732.5 L^{-1} at an
9 altitude of $\sim 9.6 \text{ km}$ with the majority of particles sized between 50 and 100 μm and a small number of particles
10 larger than 100 μm . Above this layer, three layers (CL3, CL4 and CL5) of cirrus clouds (as the temperature is below
11 $-40 \text{ }^\circ\text{C}$) are observed having low concentrations (less than 10 L^{-1} in CL3 and CL4 and less than 200 L^{-1} in CL5) of
12 ice crystals. In CL3, ice crystals are smaller than 100 μm and in CL4 they are smaller than 40 μm . CL5 is a
13 subvisible (optical thickness at 532 nm of ~ 0.025) cirrus cloud layer located at the CPT. The CPT is located at an
14 altitude of about 17.9 km having ~~an extremely cold~~ temperature of about $-86.4 \text{ }^\circ\text{C}$ (Fig. 2b). CL5 has a geometrical
15 thickness of about 2.1 km with its top located at $\sim 18.3 \text{ km}$ in the lower stratosphere, $\sim 400 \text{ m}$ above the CPT. Note
16 that the peak in BSR_{940} and peaks in particle concentration corresponding to the 5 and 10 μm size bins are located
17 exactly at the CPT. CL5 consists of particles smaller than 50 μm with most of the particles smaller than 25 μm . This
18 tropopause cirrus is again detected by the COBALD during the descent flight between 21:49 UTC and 21:51 UTC at
19 almost similar altitude and similar temperature nearly 100 km southwest from the location of CL5 as shown in Fig.
20 3(a). About five hours later, a similar tropopause cirrus cloud layer was noticed in the CATS lidar observations as
21 discussed in the next section. In the subsequent sections we discuss the properties of CL5.

22 3.2 CATS lidar observations of the tropopause cirrus cloud layer

23



1



1
2
3 **Figure 3:** (a) ERA5 **temperature** **cloud-cover fraction** at 100 hPa on 24 August 2017 averaged between 01:00
4 and 02:00 UTC. CATS overpass is shown by solid blue line with filled red circles superimposed on it
5 representing the locations of cirrus clouds with base height greater than 16 km. Solid black line shows the
6 balloon flight trajectory from TIFR-BF on 23 August 2017 (shown by red plus sign) with red circles
7 representing the locations of cirrus clouds with base altitude above 16 km during the ascent (at around 20:46
8 UTC) and descent (at around 21:50 UTC). Dashed lines show the forward trajectories from the location of
9 tropopause cirrus at 16.8 km (purple), 17.8 km (magenta) and 18.3 km (orange), respectively. (b) Vertical
10 profiles of scattering ratio obtained from CATS (at 1020 nm wavelength) and COBALD (at 940 nm
11 wavelength) measurements. CATS profiles are averaged between 17.40° N and 17.65° N region along its orbit
12 track. (c) **Vertical profiles of relative humidity with respect to ice (RH_i) from ERA5 during the ascent (2100**
13 **UTC) and descent (2200 UTC). The vertical dashed blue line marks 100% relative humidity with respect to**
14 **ice.**

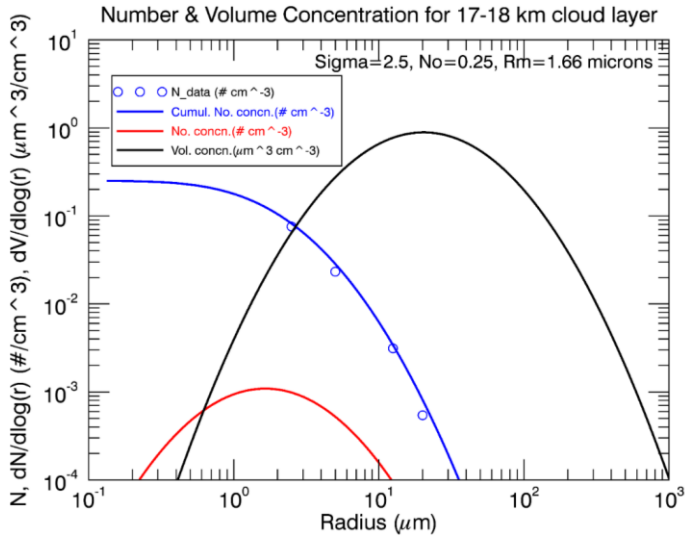
15
16 On 24 August 2017 at about 01:36 UTC (~5 hours after CL5 detection), there was an overpass of the ISS nearly 100
17 km west from the location of the tropopause cirrus cloud detected during the balloon descent flight and ~200 km
18 from TIFR-BF. This allowed us to corroborate our balloon observations using the onboard operational CATS lidar
19 data. Linking the data to its larger regional context, Fig. 3(a) shows a colour contour map of mean cloud cover
20 fraction from ERA5 reanalysis data at 100 hPa pressure level (altitude ~16.8 km) pressure level between 01:00 UTC

1 and 02:00 UTC on 24 August 2017. Both balloon (ascent and descent) and CATS measurements of clouds with base
2 altitudes above 16 km at different times and different locations along the wind direction confirm the large horizontal
3 extent of the tropopause cirrus cloud. The horizontal extent of this cloud layer along the CATS orbit track is found
4 to be more than 500 km (Fig. S2).

5 We further run forward trajectories using HYSPLIT model initialized ~~at from three~~ different altitudes
6 ~~of within~~ the CL5 to see whether the cirrus cloud layer detected by CATS is influenced by the same air mass or not.
7 ~~These altitudes correspond to the locations in the vicinity of CL5 base altitude (16.8 km), the CPT (17.8 km), and~~
8 ~~the top altitude (18.3 km) of CL5.~~ These trajectories ~~are intersected by~~ the CATS orbit track between 17.40 °N and
9 17.65 °N ~~after ~2.5 hours of the passage of air-parcels coming from the CL5, indicating their possible influence.~~ The
10 mean vertical profiles of the backscattering ratio and total depolarization ratio at 1064 nm from the CATS lidar
11 averaged between 17.40 °N and 17.65 °N along its orbit track are shown in Fig. 3(b) along with the backscattering
12 ratio profiles from COBALD at 940 nm during the ascent and descent. Although these measurements are at different
13 time, locations and wavelengths, a good qualitative agreement can be seen between the two measurements as far as
14 cirrus clouds near the tropopause are concerned. The value of total depolarization ratio at 1064 nm from the CATS
15 lidar lying between 0.4 and 0.5 confirms that this cloud layer consists of non- spherical ice crystals. The CATS
16 cloud phase algorithm also classifies this layer as an ice-cloud layer (Fig. S2). Daily radiosonde observation at 00
17 UTC from IMD Hyderabad station (17.45 °N, 78.46 °E) just before the ISS overpass on 24 August 2017 revealed
18 that the CPT altitude is about 17.7 km (Fig. 3b) while the CPT temperature is found to be coldest (about -81.5 °C) in
19 the last one week. This tropopause cirrus cloud layer is the focus of this manuscript, and we discuss about its
20 microphysical (ice crystal number concentration, effective diameter, and ice water content) and optical properties
21 (extinction coefficient and lidar ratio) derived from our balloon measurements in the following section (Sect. 3.3).
22 We also investigate and discuss the mechanisms responsible for its formation in Sect. 3.4.

24 3.3 Microphysical and optical properties of the tropopause cirrus cloud

25 We got only four altitude bins within the CL5 at 100 m resolution where the estimation of microphysical properties
26 using the size distribution is possible. This is because ice crystals were counted only in a few size bins away from
27 the CPT as shown in Fig. 2(c) and particle concentration in at least four size bins are needed for the solution to
28 converge. Assuming spherical ice crystals in CL5, the log-normal size distributions for particle number and volume
29 concentrations at each of these altitude bins are obtained. Figure 4 shows such distributions for the layer mean
30 particle concentration in CL5. From the size distribution, we derive various parameters as discussed below.



1
2 **Figure 4: Particle size distribution of the cloud layer (CL5) observed between 17 and 18 km from the Boulder**
3 **Counter measurements on 23 August 2017. Particle number concentration and volume concentration are**
4 **shown by solid red and black lines, respectively. Measured cumulative number concentration is shown by**
5 **open blue circles while the solid blue line is log-normal fit to it. The width of the distribution is given by**
6 **Sigma, which is about 2.5, total particle concentration (N_0) in the mode is 0.25 per cm^{-3} and $R_m = 1.66 \text{ } \mu\text{m}$ is**
7 **the median radius.**

8 9 3.3.1 Ice crystal number concentration (N_{ice})

10 As shown in Fig. 4, the cumulative ice crystal number concentration for CL5 derived from the log-normal
11 distribution (blue curve) fits well with the measured cumulative number concentration (blue circles). The mean
12 particle number concentration (for diameter $> 5 \text{ } \mu\text{m}$) inside the CL5 layer is about 46.79 L^{-1} with a maximum
13 concentration of $\sim 196.3 \text{ L}^{-1}$ at the CPT (Fig. 2c). Particle concentration at different altitude bins within CL5 are
14 given in Table 2+. These values are in good agreement with those measured inside tropopause cirrus clouds under
15 similar temperatures observed over Bandung, Indonesia (Shibata et al., 2012), the Western Pacific (Woods et al.,
16 2018) and Costa Rica (Lawson et al., 2008).

17 18 3.3.2 Effective diameter (D_e)

19
20 Using equation (3), the effective diameter (D_e) of ice crystals within CL5 at different altitude bins from 17.3 km to
21 17.7 km are estimated and are shown in Table 4.2. We have integrated between the radius from 1 to 25 μm because
22 we do not see ice particles larger than 50 μm (diameter) in CL5. D_e varies between 16.34 and 26.61 μm with a
23 mean plus/minus a standard deviation of $20.22 \pm 4.54 \text{ } \mu\text{m}$. The mean effective diameter for CL5 between 17.3 and

1 17.7 km obtained from temperature using equation (4) is about $18.01 \pm 0.49 \mu\text{m}$ while the value obtained using
2 equation (5) (i.e., for temperatures between $-81.32 \text{ }^\circ\text{C}$ and $-85.76 \text{ }^\circ\text{C}$) is found to be about $21.29 \mu\text{m}$ ~~which is in~~
3 ~~good agreement with that obtained from the size distribution.~~ D_e estimated from equation (3) exhibits an increase in
4 ~~its magnitude with decreasing temperature which is contrary to that observed in case of D_e estimated from~~
5 ~~equations (4) and (5).~~ Increase in D_e estimated from equation (3) is also consistent with increase in particle
6 ~~concentration with gradually increasing contribution coming from larger particles (diameter $> 25 \mu\text{m}$) near the~~
7 ~~tropopause as shown in Table 2 and Fig. 2c.~~ The effective diameter for the tropopause cirrus cloud layer observed
8 between 17 and 18 km at temperatures below $-83 \text{ }^\circ\text{C}$ by Shibata et al. (2007) was in the range from 8 to $80 \mu\text{m}$.
9 Whereas the ATTREX data showed that the median value of D_e reaches near $12 \mu\text{m}$ at temperatures below $-86 \text{ }^\circ\text{C}$
10 (Thornberry et al., 2017).

12 3.3.3 Extinction coefficient (σ_{ext})

14 The values of the extinction coefficients estimated using relation (6) at different altitude bins within CL5 are given
15 in Table 2. The mean and standard deviation of σ_{ext} ($0.028 \pm 0.009 \text{ km}^{-1}$) are slightly higher than the value
16 $0.018 \pm 0.005 \text{ km}^{-1}$ obtained from the FOV corrected COBALD backscatter coefficient derived at 532 nm wavelength
17 using a constant lidar ratio of 22 sr. This value of lidar ratio is chosen based on the CALIOP L2 V4 algorithm
18 following Young et al. (2018), where the initial lidar ratio at a cloud centroid temperature (for CL5) of about -81.4
19 $^\circ\text{C}$ is about 22 sr. The lower value of the extinction coefficient derived from COBALD could be due to the choice of
20 constant lidar ratio.

22 3.3.4 Lidar ratio

24 ~~The ratio of extinction to backscatter coefficient, often called the lidar ratio, is used in retrieving extinction~~
25 ~~coefficient from the backscatter measurements of elastic backscatter lidars. The retrieved extinction coefficient and~~
26 ~~hence the layer optical thickness are very sensitive to the magnitude of the lidar ratio used in the extinction retrieval,~~
27 ~~which depends on the number concentration, size and shape distributions and refractive index of the particles~~
28 ~~(Aekermann, 1998). Since microphysical properties of cirrus clouds mainly depend on temperature and RHi~~
29 ~~(Heymsfield et al., 2017), it is essential to study the dependence of lidar ratio on these factors. The variation of lidar~~
30 ~~ratio within a cirrus cloud layer can be measured in situ or by using inelastic lidars, such as Raman lidars (Ansmann~~
31 ~~et al., 1992; Sakai et al., 2003) or high spectral resolution lidars (Grund and Eloranta, 1990). In case of elastic~~
32 ~~backscatter lidars, for an extinction coefficient retrieval the lidar ratio is usually assumed to be constant (range-~~
33 ~~independent) inside a cirrus cloud layer. Version 3 CATS lidar clouds products use a constant lidar ratio of 28 sr~~
34 ~~over land and 32 sr over the oceans for tropical ice clouds (CATS Data Release Notes Version 3.0, 2018). This~~
35 ~~approach of using a constant lidar ratio is unable to account for the natural variability of the actual lidar ratio leading~~
36 ~~to erroneous extinction coefficient and cloud optical thickness retrievals for cirrus clouds (Saito et al., 2017). Using~~
37 ~~multi-year nighttime CALIOP two-way transmission and collocated IIR absorption optical depth at $12.05 \mu\text{m}$ for~~
38 ~~single-layer semi-transparent cirrus cloud layers over the ocean, Garnier et al. (2015) derived temperature dependent~~

1 multiple scattering factor and a corresponding temperature dependent parametrization of initial lidar ratio.
2 Following this study, the multiple scattering factor and lidar ratio in CALIOP V4 algorithm are approximated by a
3 sigmoid function of the centroid temperature of the 532 nm attenuated coefficient within the cloud layer (Young et
4 al., 2018). According to this sigmoid function, the value of initial lidar ratio for a cirrus cloud layer with centroid
5 temperature between -80°C and -90°C falls in the range of 20-22 sr. The introduction of this approach in the
6 CALIOP V4 algorithm has resulted in the reduction of the relative uncertainty assigned to the initial lidar ratio for
7 semi-transparent ice clouds by 15 % compared to V3 algorithm (Young et al., 2018).

8 There are many studies on lidar ratio of cirrus clouds using lidars measurements (see Table 5 of Voudouri et al.
9 (2020)) but such studies using in situ measurements of subvisible cirrus clouds near the tropical tropopause are rare.
10 Our unique balloon measurements provided us independent in situ measurements of backscatter (from COBALD)
11 and extinction coefficients (from Boulder Counter) inside a subvisible cirrus layer near the CPT which allowed us to
12 estimate the vertical profile of lidar ratio. Table 42 shows the value of lidar ratio inside CL5 at different altitude bins
13 between 17.3 and 17.7 km with a mean and standard deviation of about 32.18 ± 6.73 sr. In this study, the mean lidar
14 ratio is estimated for a mean temperature of $\sim -83.2^{\circ}\text{C}$ (see Table 42). To the best of our knowledge, in situ lidar
15 ratio for cirrus cloud at this low temperature has not been estimated before. Our estimates of lidar ratio are in good
16 agreement with those values (40 ± 10 sr) obtained by He et al. (2013) for cirrus clouds observed near the tropopause
17 (temperature $\sim -80^{\circ}\text{C}$) over the Tibetan Plateau during July and August of 2011. From this study, we demonstrate
18 that the combined measurements from COBALD and Boulder Counter can be used to estimate range-resolved lidar
19 ratio for optically thin cirrus cloud layer near the CPT.

Formatted: Indent: First line: 0"

21 3.3.5 Ice water content

22
23 The IWC from the size distribution information provided by the Boulder Counter data is estimated by multiplying
24 the total ice volume by ice density (917 kg m^{-3}). By assuming the spherical shape of the ice crystals, the total volume
25 is estimated from their volume distribution for ice crystal radius ranging between 1 and 25 μm . The values of IWC
26 estimated at different altitude bins between 17.3 and 17.7 km using different methods are shown in Table 42. The
27 mean and standard deviations of IWC estimated from the size distribution between 17.3 and 17.7 km is found to be
28 about $0.176 \pm 0.089 \text{ mg m}^{-3}$. We also estimated the IWC from the FOV corrected extinction coefficient obtained from
29 COBALD data by using equations (7) and (8) as shown in Table 42. Using equations (7) and (8), the mean and
30 standard deviations of IWC obtained from COBALD data are respectively found to be $\sim 0.100 \text{ mg m}^{-3}$ and 0.112 mg
31 m^{-3} , which are in good agreement with that obtained from the size distribution data. When considering the entire
32 CL5 layer, mean IWC obtained from COBALD data is found to be about 0.055 mg m^{-3} and 0.062 mg m^{-3} using the
33 relation (7) and (8), respectively. These values are within the range (0.001 - 10 mg m^{-3}) of the IWC for cirrus clouds
34 observed under similar temperature conditions (-90°C and -80°C) during several field campaigns over different
35 regions of the globe (Lawson et al., 2008; Krämer et al., 2016; Heymsfield et al., 2014; Jensen et al., 2017; Woods et
36 al., 2018; Thornberry et al., 2017). The IWC (based on the parametrization relation 7) obtained from the CATS lidar
37 observations between 17 and 18 km altitude, a few hours later of our measurements, is in the range of 0.1 - 0.6 mg m^{-3}

³. COBALD and CATS measurements are of the same order, but it is noted that these measurements are at different wavelengths, different sensitivity levels, different times, and locations. Overall, our measurements are within the range of IWC measured for cirrus clouds in similar temperature range over other regions using aircrafts and space-borne lidar. In the next section, we investigate the formation mechanisms of CL5.

Table 42: Optical and microphysical properties of CL5 derived using COBALD and Boulder Counter measurements on 23 August 2017 from TIFR-BF. Data in *italic* fonts show the properties derived using only Boulder Counter data while data shown in normal fonts are derived from COBALD and/or iMet-1 radiosonde data.

Formatted: Line spacing: 1.5 lines, No page break before

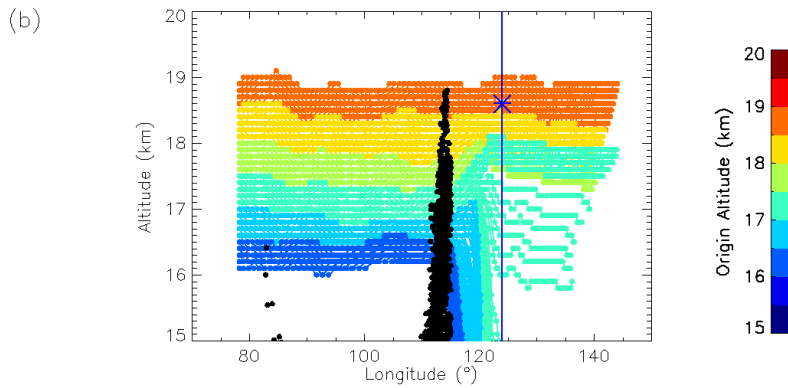
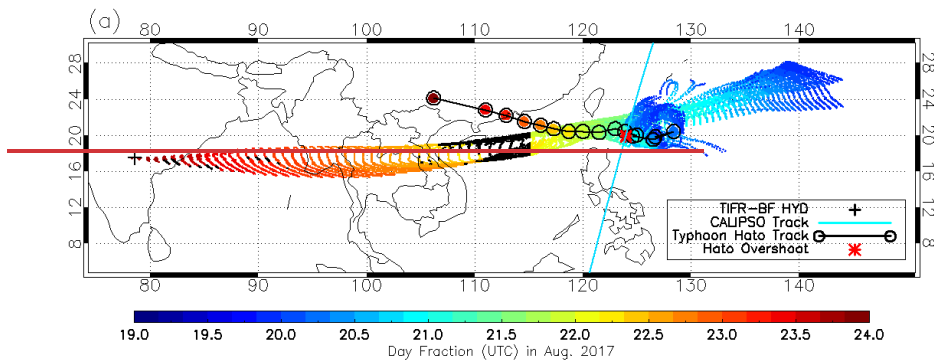
Altitude (km)	17.3	17.4	17.5	17.6	17.7	Mean \pm Std. dev.
Temperature ($^{\circ}$ C)	-81.32	-82.26	-83.23	-84.10	-84.94	-83.17 \pm 1.43
<i>No. concentration (#/L)</i>	<i>54.23</i>	<i>67.27</i>	<i>99.47</i>	<i>101.77</i>	<i>108.87</i>	<i>85.32\pm25.12</i>
<i>D_{e#} (μm) using Eqn. 3</i>	<i>16.34</i>	-	<i>17.81</i>	<i>20.11</i>	<i>26.61</i>	<i>20.22\pm4.54</i>
D _{e#} (μ m) using Eqn. 4	18.62	18.36	18.0	17.68	17.41	18.01 \pm 0.49
D _{e#} (μ m) using Eqn. 5	33.33	25.14	18.56	15.42	14.0	21.29 \pm 7.98
σ_{ext} (km^{-1}) from COBALD	0.013	0.018	0.017	0.018	0.026	0.018 \pm 0.005
<i>σ_{ext} (km^{-1}) using Eqn. 6</i>	<i>0.014</i>	-	<i>0.029</i>	<i>0.032</i>	<i>0.035</i>	<i>0.028\pm0.009</i>
β_{p532} ($\times 10^{-4} km^{-1}sr^{-1}$)	5.77	8.13	7.71	8.33	12.06	8.40 \pm 2.28
Lidar ratio (sr)	24.17	-	37.44	38.04	29.05	32.18 \pm 6.73
IWC ($mg m^{-3}$) using Eqn. 7	0.072	0.099	0.093	0.098	0.140	0.100 \pm 0.025
IWC ($mg m^{-3}$) using Eqn. 8	0.130	0.137	0.096	0.087	0.114	0.112 \pm 0.021
<i>IWC ($mg m^{-3}$) from the size distribution</i>	<i>0.070</i>	-	<i>0.157</i>	<i>0.195</i>	<i>0.285</i>	<i>0.176\pm0.089</i>

3.4 Investigation of the mechanisms involved in the formation of the tropopause cirrus

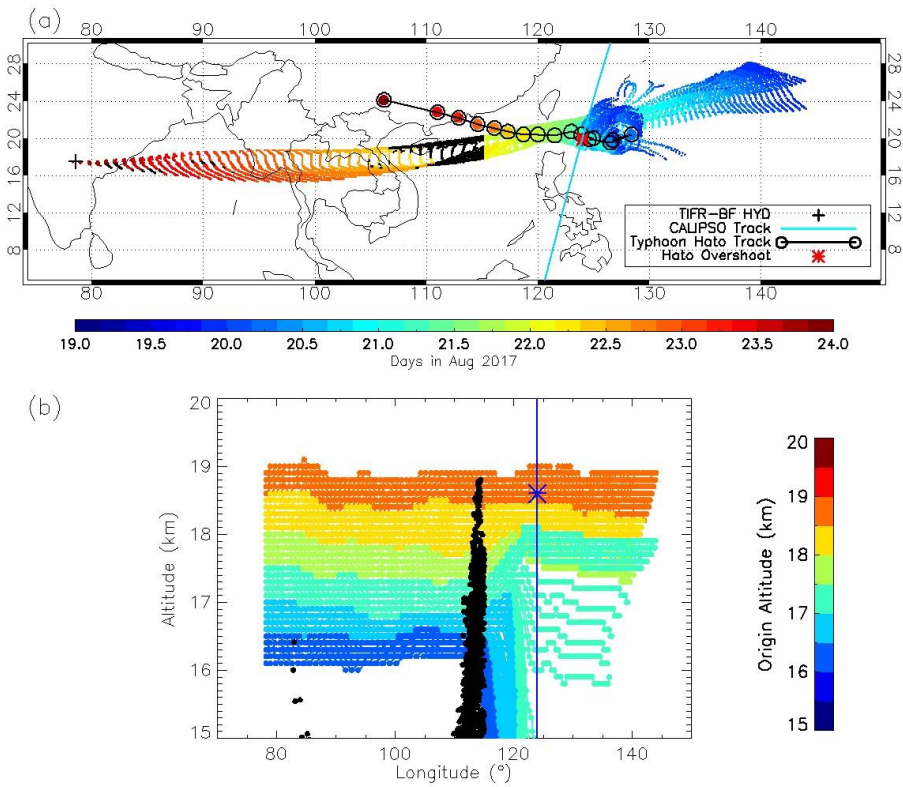
3.4.1 Back-trajectories and their intersection with deep convective clouds observed from Himawari-8

1 Overshooting convection can directly inject ice crystals into the lowermost stratosphere region (Corti et al., 2008;
 2 Khaykin et al., 2009; Dessler et al., 2016; Smith et al., 2017; Lee et al., 2019; Khaykin et al., 2022). Under the
 3 subsaturated conditions of the stratosphere, these ice crystals subsequently undergo sedimentation and sublimation
 4 leading to a hydration patch (Jensen et al., 2020; Lee et al., 2019). This hydration patch could get advected and
 5 further lead to secondary ice formation upon cooling near the CPT region. Extreme convective clouds (cloud top
 6 heights exceeding 17 km) can also induce cooling near the tropopause (Kim et al., 2018) which eventually could
 7 cause dehydration through ice formation. In addition to this, rapid tropopause cooling can also be caused by the
 8 convectively induced gravity waves (Kim and Alexander, 2015; Kim et al., 2016) followed by supersaturation, cloud
 9 formation and dehydration (Dzambo et al., 2019; Schoeberl et al., 2015, 2016). A recent study (Dzambo et al., 2019)
 10 over Australia has shown that the magnitude of tropopause cooling is greater during the monsoon period than that
 11 during the non-monsoon periods. CL5 could possibly be a result of the direct injection of ice crystals due to
 12 overshooting convection or through cooling caused by one of these processes mentioned above.

13



14



1
 2 Figure 5: (a) Five-day back-trajectories initialized on 23 August 2017 at 20:00 UTC from the balloon
 3 measurement locations at different altitudes between 16 and 19 km represented by colored dots as a
 4 function of latitude and longitude with colour showing the days in August 2017-fraction. The locations of deep
 5 convective anvil tops observed after 21 August 2017 from the Himawari-8 brightness temperature images at
 6 10.4 μm wavelength channel that intersected the back-trajectories are shown by black dots. Typhoon *Hato*
 7 track is shown by black outlined coloured circles connected by black line with colour showing the day
 8 fraction. The night-time CALIPSO orbit track on 20 August 2017 between 17:27 and 17:40 UTC is shown by
 9 cyan line with the location of the overshooting cloud top shown by red asterisk. (b) Five day back-trajectories
 10 represented as a function of longitude and altitude with colour showing their origin altitude. The locations of
 11 the anvil top altitude that intersected with the back-trajectories are represented by black dots. The locations
 12 of CALIPSO overpass and the overshooting cloud top altitude are shown by blue vertical line and blue
 13 asterisk, respectively.

14
 15 The influence of deep convection on the CL5 is investigated by using a combination of back-trajectory
 16 analysis and cloud-top brightness temperature observations at 10.4 μm from the Himawari-8 geostationary satellite
 17 data as discussed in Sect. 2.43.3+. Figure 5(a) shows five-day back-trajectories initialized from the balloon
 18 measurement sites between 16 and 19 km as a function of latitude, longitude, and time. The locations of the

1 convective anvil tops that intersected these air parcels are also superimposed along the back-trajectories. Few
2 isolated localized convective clouds over the Indian East Coast along the back-trajectories can be noticed in Fig.
3 5(a). While intersecting with the back-trajectories, the anvil top of these convective events does not reach 18 km
4 altitude. But comparisons of GOES-16 (nearly identical to Himawari-8) and Visible Infrared Imaging Radiometer
5 Suite (VIIRS) temperature (Khlopenkov et al., 2021) show that pixel resolution has a strong impact on observed
6 temperatures within convection. Therefore, the highest overshooting tops likely exceeded 18 km height. The
7 convective clouds near the Indian East Coast were also observed by the India Meteorological Department Doppler
8 Weather Radars located at Machilipatnam (16.12° N, 81.09° E) after 12:00 UTC on 23 August 2017 with maximum
9 echo altitude reaching about 17 km (Fig. S3). These convective clouds were at their peak altitudes at around 11:40
10 UTC as seen in the Himawari-8 images, and we do not have radar images prior to 12:00 UTC or co-located
11 CATS/CALIOP observations to confirm this. However, the intersection of air parcels with these convective clouds
12 over the Indian East Coast took place nearly 6 hours later at around 16:00 UTC during which their anvil top altitude
13 reduced. Based on the Himawari-8 images and back-trajectories, the direct injection of ice crystals by these local
14 convective clouds up to 18 km altitude along the Indian East Coast seems likely. Thus, we cannot fully rule out the
15 influence of local convection because we notice enhanced WVMR at 70 hPa pressure level on 23 August 2017 at
16 12:00 UTC over the surrounding regions of Hyderabad and the east Coast (see Fig. S3). This enhanced water vapour
17 might be associated with these convective clouds as far as the recent studies on the convective hydration are
18 concerned (Jensen et al., 2020; Ueyama et al., 2018). Enhanced water vapour might have led to the secondary ice
19 formation after undergoing through cold tropopause conditions while subsequent advection towards Hyderabad by
20 the TEJ. Ueyama et al. (2018) showed that the deep convective clouds occurring above 380 K potential temperature
21 level (~17 km) increase in situ formed cirrus clouds by 38 % compared to 21 % by the convective clouds in the
22 range 375-380 K. This could be the case for CL5.

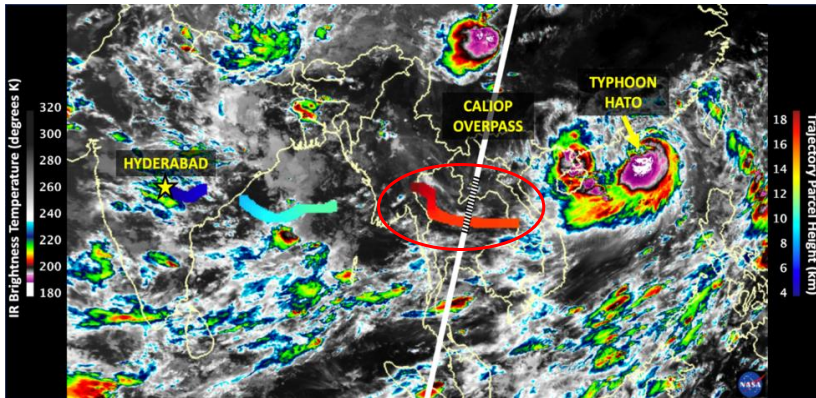
23 In addition to the hydration, these convective clouds could have also caused cooling near the CPT as
24 discussed by Kim et al. (2018), which could have facilitated the in situ formation of ice crystals. Temperature
25 measurements on 23 August 2017 at different times in and around 400 km radius of TIFR-BF suggest that such
26 cooling has most likely taken place before the arrival of the air parcels as shown in Table 23. Lack of accurate RHi
27 and ice measurements near the CPT over these convective clouds preclude us from confirming in situ formation.
28 Thus, the role of local deep convective clouds in the formation of CL5 is not quite clear due to the lack of
29 observations. High-resolution model simulations of these convective clouds could help in ascertaining their role in
30 the formation of tropopause cirrus clouds, which is beyond the scope of this study.

31
32

Table 32: Variation of the CPT temperature and altitude as measured by radiosondes and GNSS-RO in and around Hyderabad during 23 and 24 August 2017.

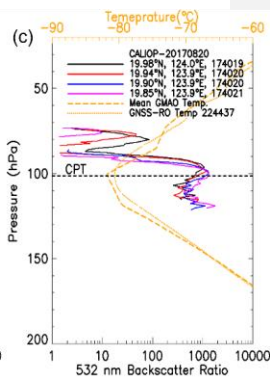
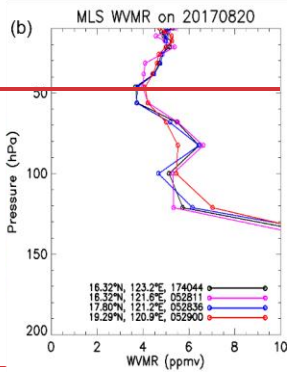
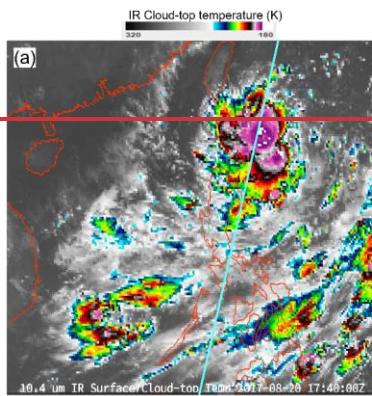
Date/Time	23 Aug 2017, 00 UTC (Radiosonde)	23 Aug 2017, ~14:00 UTC (GNSS-RO)	23 Aug 2017, 20:55 UTC (Radiosonde)	23 Aug 2017, 21:50 UTC (Radiosonde)	24 Aug 2017, 00 UTC (Radiosonde)
Location	17.45° N, 78.46° E	18.45° N, 81.40° E	17.44° N, 78.30° E	17.40° N, 77.36° E	17.45° N, 78.46° E
Distance from TIFR-BF (km)	13.5	332	38.9	135.5	13.5
CPT altitude (km)	17.20	17.30	17.9	17.75	17.7
CPT temperature (°C)	-77.2	-82.5	-86.4	-86.1	-81.5

In Fig. 5(a), we note that the air parcels have already been influenced by deep convective clouds over the South China Sea before their intersection with local convective clouds over the Indian East Coast. The altitude distribution of the back-trajectories shown in Fig. 5(b) suggests that the air parcels initialized from the balloon measurement altitudes between 16 and 18 km have originated from the lower levels (below 10 km) in the region between 115° E and 125° E on 22 August 2017. This large-scale upward movement of the air parcels indicates a synoptic scale convective system, such as a tropical cyclone or a typhoon. Himawari-8 brightness temperature image on 22 August 2017 at 19:00 UTC in Fig. 6 does reveal such synoptic scale system named typhoon *Hato*, a category-3 tropical cyclone in the South China Sea, which severely affected the coastal cities of Macau, Zhuhai, and Hong Kong in southern China on 23 August 2017 after its landfall (Li et al., 2018). Typhoon *Hato* intensified to a category-3 typhoon just before its landfall (Pun et al., 2019) and it was one of the strongest typhoons in the last several decades, which caused widespread flooding in the Pearl River Delta region in southern China, Macau being the hardest hit city (ESCAP/WMO Typhoon Committee, 2017). The anvil cloud top altitude derived from the Himawari-8 cloud-top temperature images along the back-trajectories are found above 18.5 km (Fig. 5b) with the highest cloud top altitude of about 18.8 km observed on 22 August 2017 at 09:10 UTC over 18.85° N, 114.48° E. It appears that typhoon *Hato* had most likely injected ice crystals in the lower stratosphere as the CPT altitude observed from the nearest radiosonde temperature profile over Haikou station (20.03° N, 110.35° E) at 12:00 UTC was about 17.4 km (Fig. S4). Moreover, the tropopause temperature and tropopause altitude might be substantially reduced by the overshooting convection as pointed out by Sun et al. (2021).

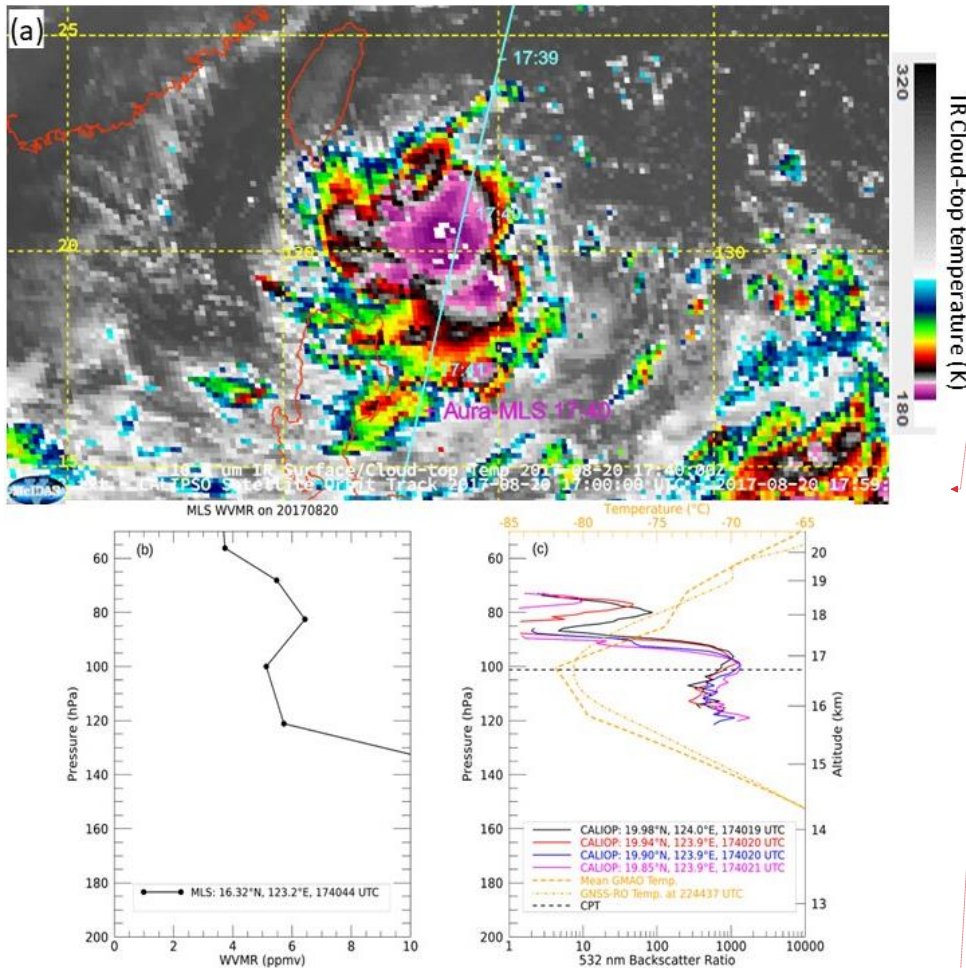


1
2 **Figure 6: Image of brightness temperature (in Kelvin) at 10.4 μm infra-red channel of Himawari-8 satellite**
3 **valid for 22 August 2017 at 19:00 UTC over East Asia. Typhoon *Hato* is associated with very low brightness**
4 **temperature. The altitudes (in km) of back-trajectory air-masses initialized from the balloon measurement**
5 **site (Hyderabad, India; denoted as yellow star) are superimposed on the image and are represented by thick**
6 **coloured curves. The air-mass back-trajectories initialized between 16 and 18 km altitude above Hyderabad**
7 **at the time of the balloon flight on 23 August 2017 are encircled red. The thick white line shows the night-**
8 **time CALIPSO overpass from 19:06 to 19:20 UTC on 22 August 2017 with black stripes showing the region**
9 **where tropopause cirrus was sampled.**
10

11 Ice crystals injected by typhoon *Hato* in the subsaturated lower stratosphere might have caused a hydration
12 patch after undergoing through sedimentation and sublimation while being advected westward by the prevailing
13 easterly winds. The ERA5 WVMR at 70 hPa pressure level on 22 August 2017 at 09:00 UTC indeed reveals such
14 hydration patch (see Fig. S4). We did not have collocated CATS/CALIOP observations at that time to verify this
15 overshooting event. However, there was a nighttime CALIPSO overpass on 20 August 2017 through the developing
16 typhoon between 17:28 UTC and 17:40 UTC (a few hours before the passage of the air parcels) that observed cloud
17 top altitude of about 18.6 km (see Fig. 5a, 5b and Fig. S5). Daytime and co-located night-time profiles of the
18 WVMR from the MLS instrument confirm the presence of such hydration over typhoon *Hato* with peak WVMR
19 reaching ~ 6.5 ppmv at 82.5 hPa pressure level near the tropopause (Fig. 7b). The location of the clouds observed by
20 CALIOP is well above the CPT observed from the nearest GNSS-RO temperature profile at 22:44 UTC as shown in
21 Fig. 7c. This WVMR value could be even higher after *Hato* intensified to a category-3 typhoon because
22 intensification is followed by frequent long-lasting intense convective bursts (Horinouchi et al., 2020) that increase
23 the possibility of overshooting and direct hydration in the lower stratosphere (Romps and Kuang, 2009; Jiang et al.,
24 2020). Aircraft observations over the Western Pacific region during the NASA's POSIDON campaign have
25 provided evidence for such direct hydration in the outskirts of typhoon *Haima* on 15 October 2016 (Jensen et al.,
26 2020). They observed a layer (~ 1 km thick) of enhanced water vapour in the lower stratosphere with a peak WVMR
27 of about 7 ppmv at an altitude of ~ 17.5 km, which could not be resolved by MLS owing to its coarse vertical
28 resolution (see Fig. 2 of Jensen et al. (2020)).



1



Formatted: Font: 12 pt

Formatted: Normal (Web), Centered, Indent: First line: 0", Line spacing: single

1
2 Figure 7: (a) 10.4 μm infrared cloud-top temperature from Himawari-8 at 17:40 UTC on 20 August 2017
3 showing the overshoots during the development phase of typhoon *Hato*. The cyan line represents the
4 CALIPSO orbit track that observed the overshoot on 20 August 2017 between 17:2740 and 17:410 UTC while
5 the magenta plus symbol denotes the location of Aura-MLS profile at 17:40 UTC. (b) Co-located vertical
6 profiles of water vapour mixing ratio (WVMR) from MLS on 20 August 2017 at 17:40 UTC near the
7 overshoot region observed during daytime and the night-time overpasses of Aura satellite. (c) Vertical
8 profiles of 532 nm backscatter ratio obtained from the CALIOP on 20 August 2017 at around 17:40 UTC.
9 Dashed orange lines show the mean temperature profile obtained from GMAO along the CALIPSO track
10 and from GNSS-RO at 22:44 UTC. Dashed horizontal black line represents the CPT.

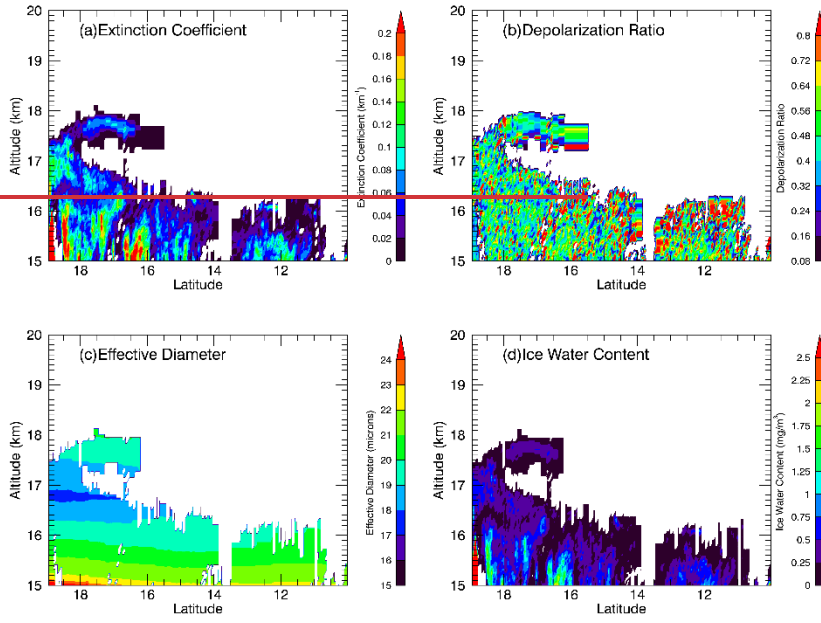
Formatted: Font: Bold

11

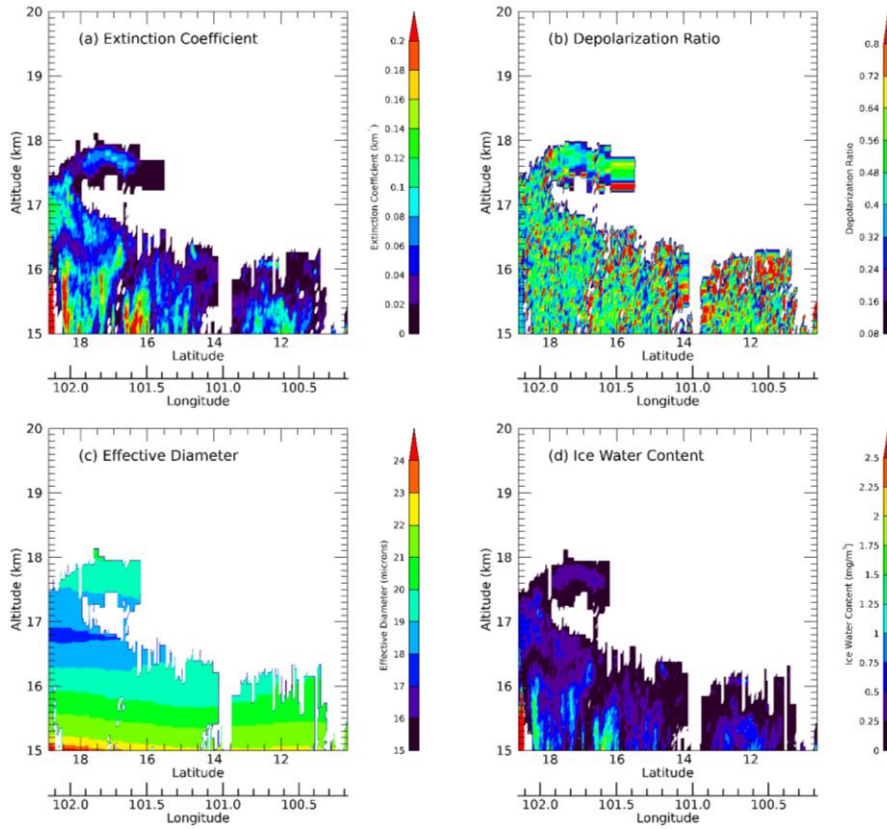
1 Jiang et al. (2020) have studied the impact of 30 tropical cyclones (TC, many of them observed during the ASM) on
2 the UTLS water vapour over the tropical northwestern Pacific Ocean using MLS and CloudSat observations during
3 2012-2016. They found that the lower-stratospheric water vapour over the TC area increased by an average value of
4 0.75 ppmv compared to the non-TC area, indicating direct hydration. It seems that the hydration caused by typhoon
5 *Hato* has followed the anticyclonic flow and may have influenced the formation of CL5. We investigate this
6 advection with further water vapour observations from MLS and ERA5 derived WVMR in the next sub-section.
7

8 **3.4.2 Advection of injected ice and hydration caused by typhoon *Hato*** 9

10 As discussed in the previous section, the trajectories and the Himawari-8 cloud-top images suggest that the
11 ice crystals detected by our balloon measurements are likely influenced by the convective outflow of typhoon *Hato*,
12 which could possibly be advected to the measurement site by the Tropical Easterly Jet (TEJ) or formed in situ from
13 the moist air-mass (from sublimated overshoot) brought by TEJ near the cold tropopause. We discuss these aspects
14 in this section. TEJ is known to play a significant role in the redistribution of upper-tropospheric moisture and the
15 formation of cirrus clouds during the ASM (Das et al., 2011). However, it can be questioned that the ice crystals
16 sampled by our balloon measurements can survive that long distance (about 4000 km) if they were advected from
17 the outflow of a typhoon because larger particles would eventually sediment and sublimate in a subsaturated region.
18 Assuming the ice crystals to be spheroids (aspect ratio=1), the terminal velocity calculated by using the relationship
19 given by Heymsfield and Westbrook (2010) suggests that both 5 and 10 μm particles will fall less than 1 km in two
20 days. Thus, they are expected to survive within the layer if they were advected from the outflow of typhoon *Hato* by
21 the TEJ provided they do not grow, or sublimate and the background conditions remain the same. These theoretical
22 calculations are consistent with the Boulder Counter measurements which show the dominance of ice crystals
23 smaller than 25 μm in CL5 (Fig. 2c). The presence of ice crystals larger than 10 μm in the middle of the CL5 could
24 be explained by the constant growth, aggregation, and consequent sedimentation within the layer in the outflow.
25



1



1
 2 **Figure 8: Optical and microphysical properties of cirrus clouds observed by CALIOP on 22 August 2017 at**
 3 **19:00 UTC over Southeast Asia represented by black stripes in Fig. 6.**
 4

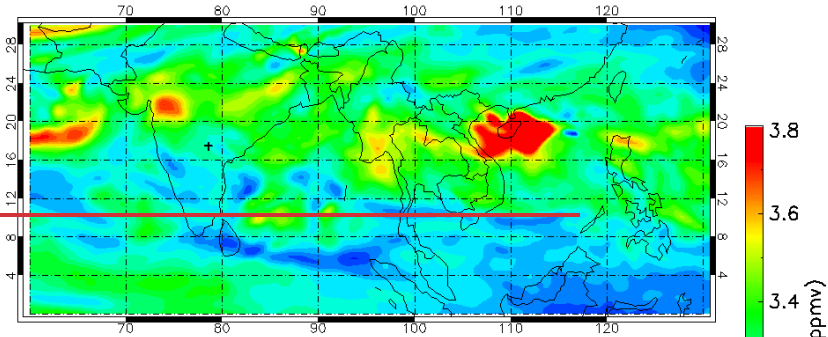
5 A thin cirrus cloud layer can be seen near the tropopause between 17 and 18 km over Laos and Thailand in
 6 the night-time observations from CALIOP on 22 August 2017 at around 19:00 UTC along the air parcels coming
 7 from the typhoon with properties like CL5 (Fig. 8a-d). This cirrus cloud layer extended horizontally to more than
 8 200 km along the CALIPSO orbit track in the same latitude band (17° N - 18° N) where the balloon measurements
 9 were taken. The values of depolarization ratio between 0.3 and 0.6 and colour ratio close to 1 (Fig. S6) in this layer
 10 confirm the presence of non-spherical ice crystals. The CALIOP IWC to extinction coefficient ratio provides an
 11 estimated effective diameter ranging between 18 and 20 μm , which is consistent with our balloon measurements
 12 ($20.22 \pm 4.54 \mu\text{m}$). The peak extinction coefficient value lies between 0.08 and 0.1 km^{-1} and is in the altitude range
 13 of 17.6-17.9 km, consistent with the extinction coefficient maxima (0.06 km^{-1} at 17.9 km from COBALD) for CL5.
 14 The IWC estimated by CALIOP for this layer using an empirical parametrization developed from aircraft data
 15 (Heymsfield et al., 2014) ranges between 0 and 0.5 mg m^{-3} . These similarities in optical and microphysical properties

1 suggest that the two layers detected by balloon and CALIOP could possibly be formed by the same mechanism
2 under similar background conditions. However, the lifetime of ice crystals in cirrus clouds depend on several local
3 background factors such as temperature, relative humidity with respect to ice, horizontal wind and updraft speed,
4 and the type and quantity of ice-nuclei. These factors may vary rapidly especially in the TTL under the influence of
5 deep convective clouds, TEJ, gravity waves, and relatively high aerosol concentration during the ASM, which could
6 influence the ice microphysics. This means that the ice crystals formed at one location through one mechanism may
7 sublimate and/or crystalize at other locations while moist air is being transported to another location depending upon
8 the local background conditions which force its distribution between ice and gas phases. It is therefore important to
9 keep a track record of these parameters along the back-trajectories. We discuss the role of background conditions
10 such as temperature, water vapour and vertical wind speed on the in situ formation of tropopause cirrus clouds along
11 the back-trajectories in the next sub-section.

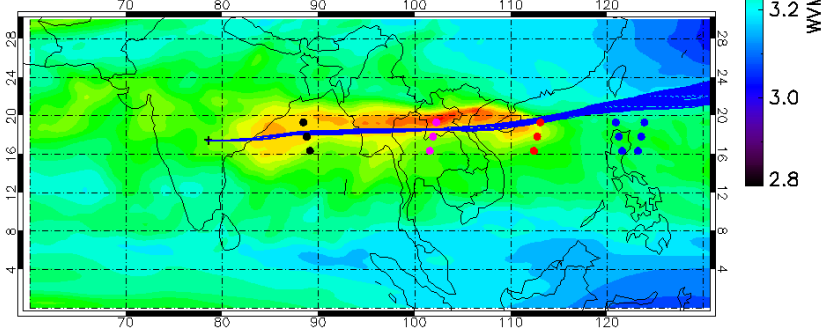
12 As mentioned earlier, the convectively injected ice by typhoon *Hato* in the subsaturated lower stratosphere
13 may undergo sedimentation and sublimation leading to a hydration patch in the lower stratosphere (Lee et al., 2019).
14 To investigate this, we derive WVMR from ERA5 relative humidity and temperature hourly data at 70 hPa over
15 typhoon *Hato* on 22 August 2017 at 09:00 UTC where the peak overshoot was observed from the combined analysis
16 of Himawari-8 and the back-trajectories (Fig. 9a). We see an enhancement in the WVMR located between 15°-20°
17 N and 107°-114° E. As we move forward in time, this enhanced moist plume is seen to be advected towards the
18 west. However, a weaker enhancement in WVMR can also be seen over the Indian East Coast surrounding
19 Hyderabad, probably due to afternoon deep convective clouds, which likely have also assisted the formation of CL5.
20 The advection of moist plume can also be seen in the averaged WVMR at 70 hPa level for 22 and 23 August 2017
21 with high WVMR between 15° N and 20° N latitudes as shown in Fig. 9(b).

22

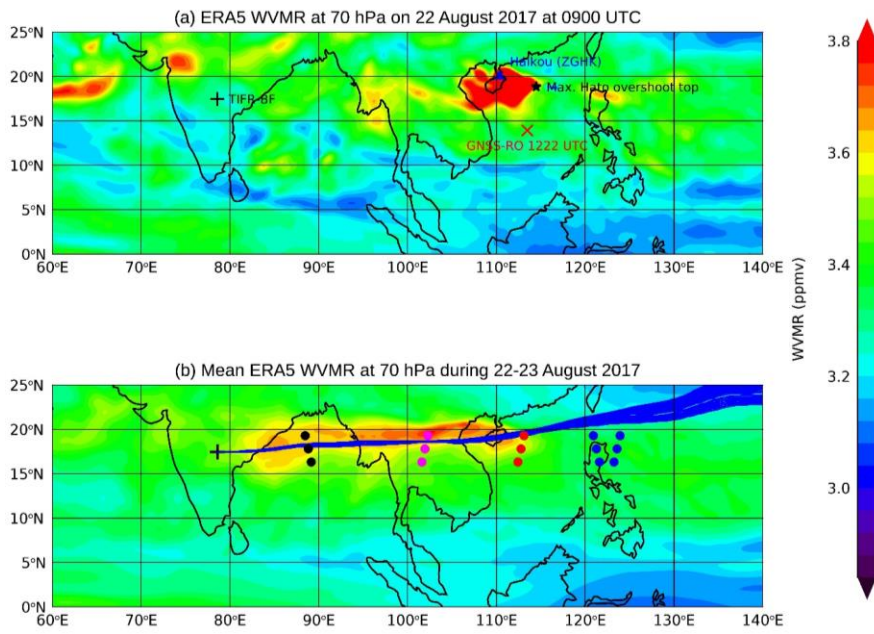
(a) ERA5 WVMR at 70 hPa on 22 August 2017 at 09 UTC



(b) Mean ERA5 WVMR at 70 hPa during 22–23 August 2017



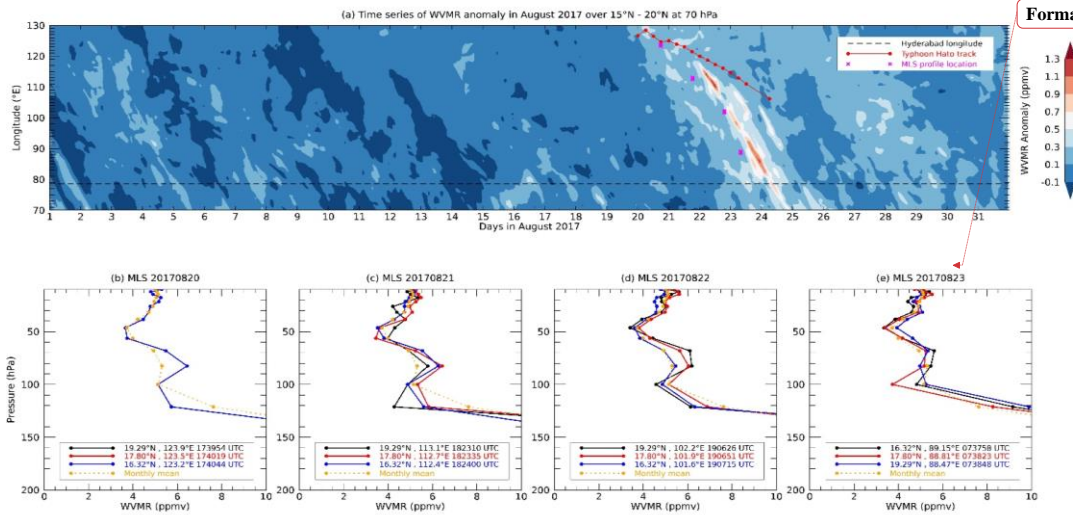
1



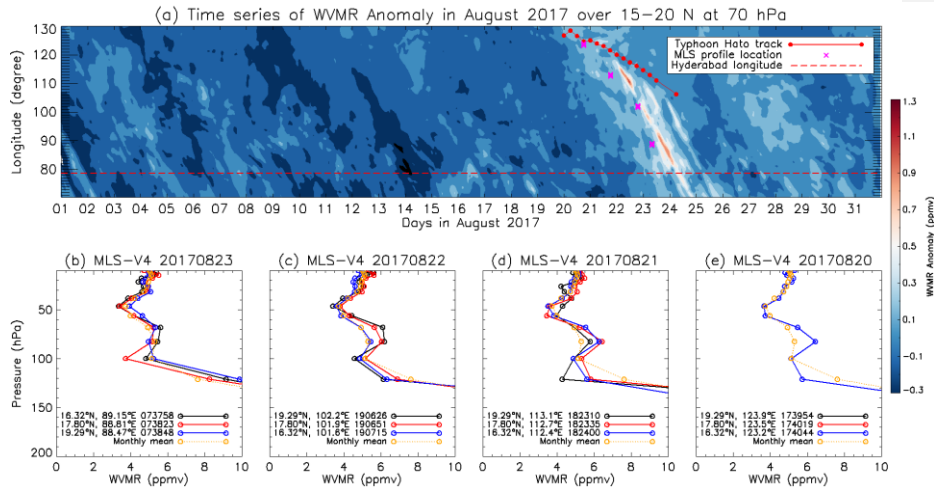
1
2
3 **Figure 9: (a) Spatial map of water vapour mixing ratio (WVMR) derived from ERA5 data at 70 hPa level on**
4 **22 August 2017 at 09:00 UTC showing large enhancement over the South China Sea. The locations of TIFR-**
5 **Balloon Facility, Haikou radio sounding station, maximum overshoot top altitude and GNSS-RO profile**
6 **obtained at 1222 UTC are represented by black plus, blue triangle, black star, and red cross symbols,**
7 **respectively.** (b) Average water vapour mixing ratio derived from ERA5 for 22 and 23 August 2017 at 70 hPa
8 with back-trajectories initialized between 18 and 19 km (between 79 and 68 hPa) from the balloon site
9 represented by blue lines superimposed on it. Nearest MLS footprints with respect to the back-trajectories
10 between 16° and 20° N on 20, 21, 22 and 23 August 2017 are represented by blue, red, magenta, and black
11 filled circles, respectively.
12

13 To quantify the transport of this enhanced moisture relative to the monthly mean WVMR at 70 hPa and
14 non-TC area, we estimated WVMR anomaly for the month of August 2017 by subtracting the mean WVMR for
15 each grid over this region (between 15° N and 20° N). The Hovmöller plot in Fig. 10 (a) clearly shows the transport
16 of enhanced moisture (0.6-0.9 ppmv) relative to the monthly mean and reaching Hyderabad on 23-24 August night.
17 We also notice that the magnitude of this enhanced moisture is in good agreement with the results found by Jiang et
18 al. (2020) using MLS observations. We also verified this transport with the MLS WVMR observations during 20
19 and 23 August 2017 over this region (between 15° N and 20° N) that transacted the back-trajectories nearest in
20 space and time (Fig. 10b). We clearly see enhanced moisture (greater than the monthly mean value) at 82.5 hPa and
21 68 hPa pressure levels whose magnitude decreases as we move forward in time (from Fig. 10e to 10b). While being
22 advected, this moist plume may get transported downward towards the CPT and may lead to in situ secondary ice

1 formation upon cooling. We present the evidence for such downward transport and cooling near the tropopause
 2 along the back-trajectories in section below.



Formatted: Centered

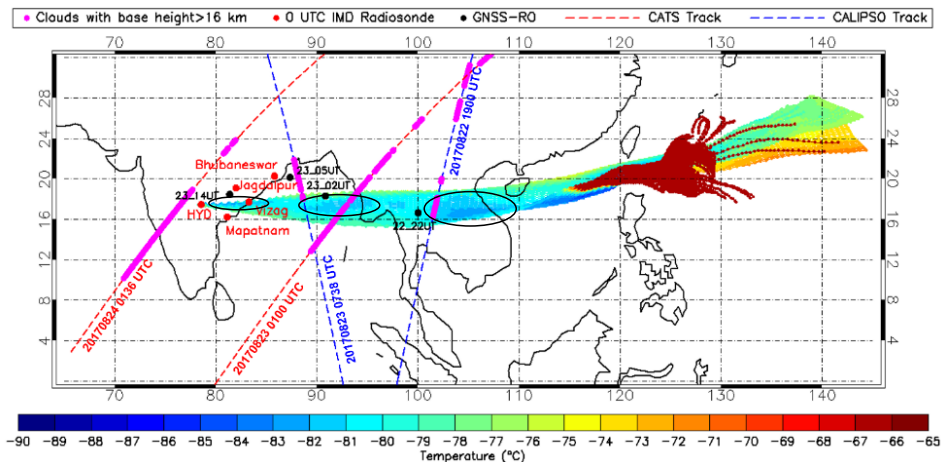


4
 5 **Figure 10: (a) Hovmöller plot for the anomaly in water vapour mixing ratio (WVMR) derived from ERA5**
 6 **temperature and relative humidity at 70 hPa pressure level for August 2017. Anomaly is computed by**
 7 **subtracting the monthly mean WVMR for each grid between 15° N and 20° N. Dashed black/red line marks**
 8 **the longitude of TIFR-BF in Hyderabad. Red dots represent the track of typhoon *Hato* while magenta crosses**
 9 **show the location of nearest MLS profiles on different dates. Vertical profiles of WVMR from MLS between**
 10 **15° N and 20° N observed on (b) 20³ August 2017, (c) 21² August 2017, (d) 22¹ August 2017, and (e) 20³**

1 August 2017 at different times in UTC shown by different colours in the legend. The profiles affected by
 2 clouds are filtered out. The orange line with orange circles in each panel represents the mean MLS profile for
 3 August 2017 obtained by averaging all profiles located in the region bounded by 15°-20° N and 70°-130° E.

4
 5 **3.4.3 In situ ice formation due to cooling induced by gravity waves associated with typhoon Hato.**
 6

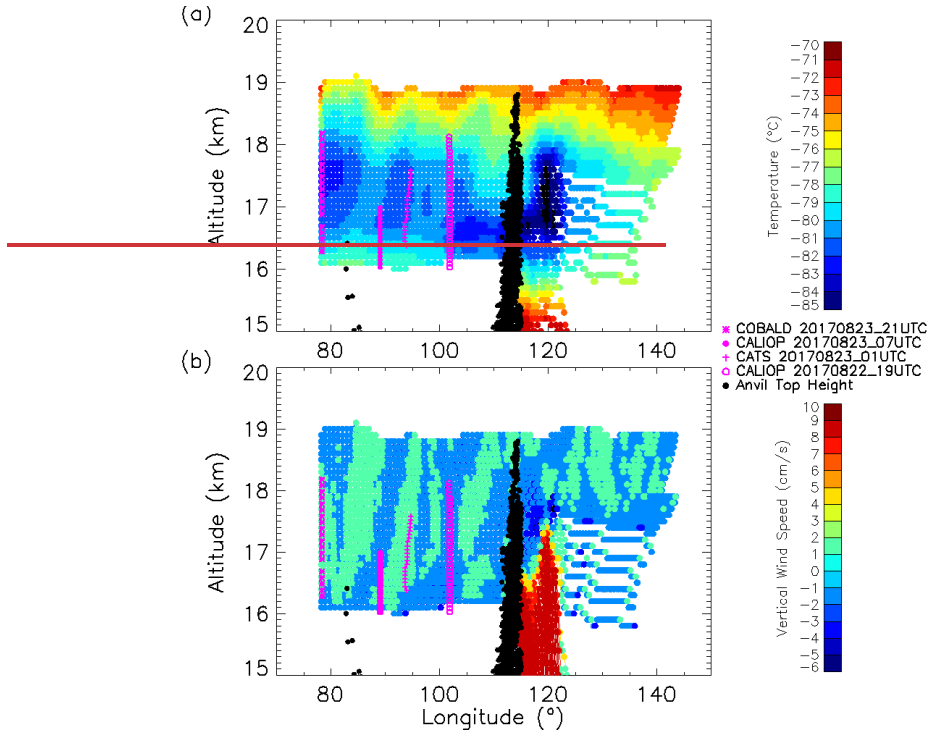
7 Figure 11 shows the temperature history of the air parcels along the back-trajectories initialized from the balloon
 8 measurement site between 16 and 19 km altitude every hour. After being influenced by typhoon Hato, the air parcels
 9 have experienced several cooling and warming phases before reaching the balloon site. We observe a quasi-periodic
 10 occurrence of cold regions (represented by encircled regions in Fig. 11) with temperature below -81 °C along the
 11 back-trajectories after being influenced by typhoon. Colder air parcels at these temperatures are susceptible to
 12 generate supersaturation that can trigger the formation of ice crystals through ice nucleation. Near coincident and co-
 13 located CATS and CALIOP observations on 22 and 23 August 2017, which intersected the back-trajectories, are
 14 used to investigate the presence of cirrus clouds in these cold-regions. CATS and CALIOP observations on 23
 15 August 2017 are almost coincident with the air parcels along the back-trajectories whereas CALIOP overpass on 22
 16 August 2017 was a few hours later to the passage of the air parcels and thus, there is a difference in time (Fig. S7). It
 17 is interesting to see the presence of cirrus cloud layers with their base altitude greater than 16 km in and around
 18 these cold regions along the CALIPSO and CATS tracks.



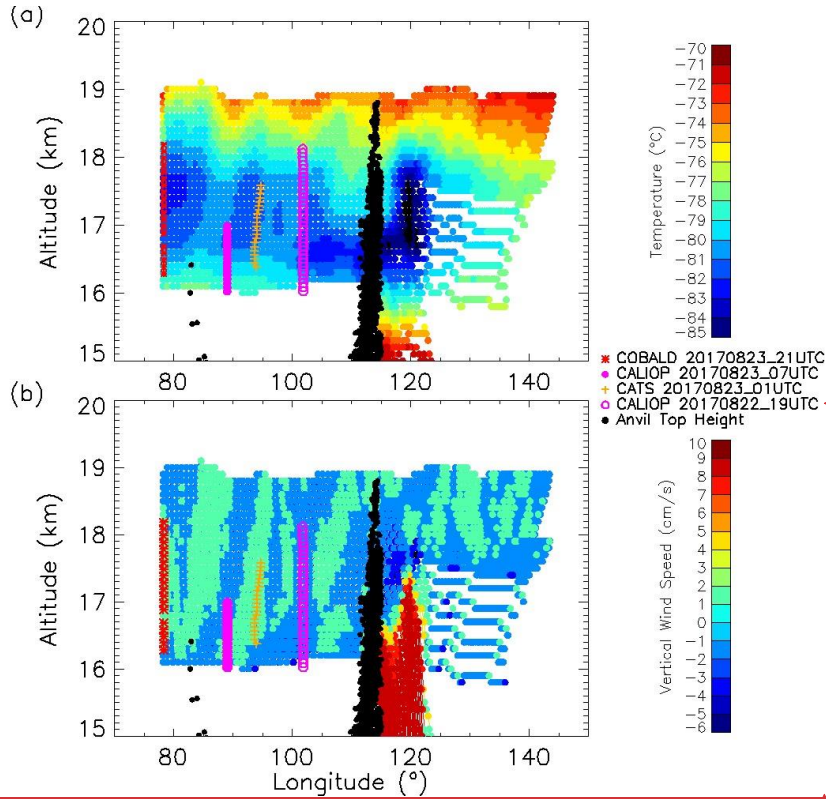
19
 20 Figure 11: Filled coloured circles on the map show the temperature and location of the air parcel at every
 21 hour along the back-trajectories run from the balloon measurement sites between 16 and 19 km on 23 August
 22 2017 at 20:00 UTC. **The encircled regions along the back-trajectories represent quasi-periodic features with**
 23 **temperature below -81 °C.** Red and blue dashed lines represent the nearest orbit tracks of CATS (on 24
 24 August 2017 at 01:36 UTC and 23 August 2017 at 01:00 UTC) and CALIPSO (23 August 2017 at 07:38 UTC
 25 and 22 August 2017 at 19:00 UTC), respectively, with respect to the air parcels. Filled magenta circles
 26 superimposed on the orbit tracks represent the locations of cirrus cloud layer with base altitude greater than
 27 16 km. Red filled circles on the map show the locations of the IMD stations from where daily radiosondes are
 28 launched at 00 UTC. Black filled circles show the locations of available GNSS-RO temperature profiles
 29 closest in time and space with CATS and CALIPSO overpasses.

Formatted: Font: Bold, Not Italic, Font color: Auto

1
2 The periodicity and the vertical extent of these cold regions can be clearly seen in Fig. 12 (a) where hourly
3 temperature along the back-trajectories initialized from the balloon site between 16 and 19 km altitude at every 100
4 m has been shown as a function of altitude (and potential temperature, see Fig. S8). The periodic cold regions are
5 confined in the altitude range between 16.5 and 18 km (potential temperature between 370 K and 400 K, see Fig.
6 S8) containing the CPT. The anvil top height derived from Himawari-8 cloud-top temperature, which intersected the
7 back-trajectories initialized between 16 and 19 km, is also superimposed (Fig. 12 a). The coldest temperatures are
8 found over the strongest updraft regions of typhoon *Hato* with highest cloud tops reaching ~18.5 km. The
9 occurrence of cirrus clouds between 16 and 18 km altitude in these cold regions is also clear from the near co-
10 located and coincident measurements from CATS and CALIOP (Fig. 12 a). We observe westward propagating
11 wave-like patterns in the temperature of the air parcels after they are influenced by typhoon *Hato*. There is also an
12 upward ~~propagation~~ movement of these wave-patterns, which are more prominent near 18 km and altitudes above
13 originating right from the region of typhoon *Hato*. Such periodic temperature fluctuations near the tropopause have
14 also been observed along the diabatic back-trajectories (derived from ERA5 data) after being influenced by a
15 typhoon observed during the ASM in a recent study (Li et al., 2020). Li et al. (2020) investigated the influence of
16 two typhoons on the dehydration and transport of low-ozone air masses near the tropopause during the ASM over
17 Kunming, China using balloon measurements of temperature, ozone, and water vapour. However, such wave-like
18 patterns in temperature and their role in cirrus cloud formation along the back-trajectories have not been discussed in
19 their study. These wave-like temperature fluctuations or temperature anomalies near the tropopause could be due to
20 the gravity waves generated by the deep convection associated with typhoon *Hato*.



1



Formatted: Font: 12 pt
 Formatted: Normal (Web), Left, Indent: First line: 0", Line spacing: single

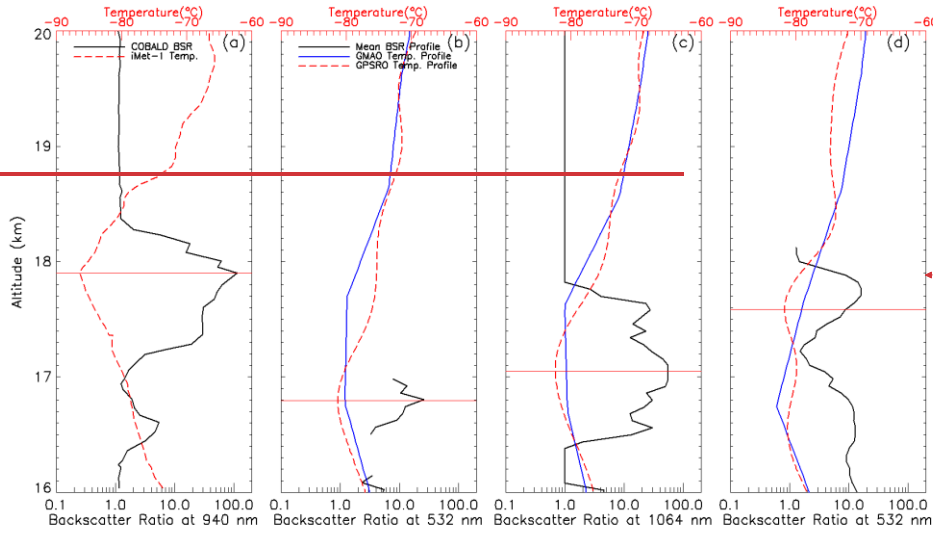
1
 2 **Figure 12:** (a) Temperature history of the air parcels along the back-trajectories run from the balloon
 3 measurement sites between 16 and 19 km on 23 August 2017. Each filled coloured circle represents
 4 temperature value at every 100 m vertical resolution at each hour. (b) Same as (top) but for the vertical wind
 5 derived from the location and time of the back-trajectories. Different **magenta coloured** symbols represent
 6 the location of the layered cirrus clouds observed near the tropopause from CALIOP, CATS and balloon
 7 measurements near co-located in space and time with respect to the back-trajectories. The locations of anvil
 8 cloud top altitude are represented by black dots.
 9

10 Using the radiosonde observations over the tropical Western Pacific region, Kim and Alexander (2015)
 11 have shown that the CPT temperature is directly modulated by the vertically propagating waves irrespective of any
 12 change in the mean upwelling. Later, Kim et al. (2016) showed ubiquitous influence of waves on the TTL cirrus
 13 clouds using airborne observations of temperature and cirrus clouds obtained over the Western Pacific during the
 14 ATTREX campaign. Several studies (Wu et al., 2015; Nolan and Zhang, 2017; Kim et al., 2009) have reported
 15 anomalies in temperature and vertical wind speed associated with semi-circular gravity waves generated from the
 16 typhoon centre propagating horizontally and vertically through the troposphere, stratosphere, and mesosphere in
 17 expanding spirals with horizontal wavelengths typically in the range of 50-500 km and periods from 1 hour to 1.6

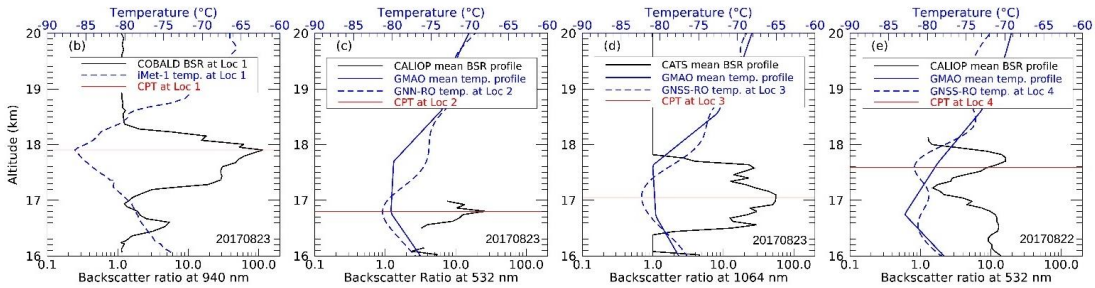
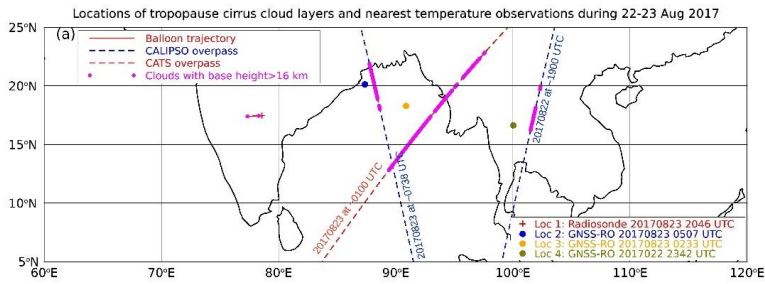
1 ~~days~~. We derived vertical wind speed along the back-trajectories (Fig. 12b) which shows correspondence between
2 the periodic updrafts and cold anomalies. This suggests that the areas of cold anomalies are most likely formed due
3 to the cooling induced by the updraft. It has been found that the updraft motion slows down the process of
4 sedimentation, leading to longer lifetime of ice crystals in cirrus clouds (Podglajen et al., 2018). The downdrafts
5 along the back-trajectories might have brought the moisture from the lower stratospheric hydration patch towards
6 the CPT, resulting in secondary ice formation. This is evident from Fig. 5(b) where air parcels that originated
7 between 17 and 17.5 km can be seen descending from higher altitudes at around 120° N. One more interesting point
8 to note is that the ascent speed of the balloon has increased from ~6 m s⁻¹ to ~8 m s⁻¹ near the tropopause region
9 (17.5-18.5 km) with its peak value at the top of CL5, above which it decreases sharply (see Fig. S9) and beyond that
10 it exhibits oscillatory behaviour with increasing amplitude. It is interesting to note the presence of downdrafts (Fig.
11 12b) and sudden drop in balloon ascent speed above the CL5 top. Such vertical wind shear near the CPT could
12 influence the ice nucleation with sudden rising motion triggering it while sinking motion inhibits it. The association
13 of cold anomalies with updrafts indicate towards the possible role of gravity wave influence, which we investigate
14 below.

15 The temperature along the back-trajectories in our analysis is obtained from the [MERRA-2GEOS-FP](#)
16 reanalysis data, which may not be accurate enough to resolve these temperature fluctuations near the CPT when
17 compared with the observations (Tegtmeier et al., 2020). To confirm the robustness of these cold anomalies, we use
18 high resolution and relatively more accurate temperature observations from GNSS-RO near these colder regions. We
19 found temperature profiles within 6 hours interval and within 400 km radius from the location of mean scattering
20 ratio profiles of CATS and CALIOP intersecting the back-trajectories between 16° N and 18° N latitude band as
21 shown in Fig. 13 (b), (c) and (d) arranged according to their observation time (from latest to farthest). The
22 temperature near the tropopause is better resolved in the GNSS-RO temperature profiles as compared to the GMAO
23 temperature profile averaged between 16° N and 18° N latitude band along the CATS and CALIOP orbit track. It is
24 clear from the scattering ratio profiles obtained from the COBALD (at 940 nm, Fig. 13 a), CALIOP (at 532 nm, Fig.
25 13 b and d) and CATS (at 1064 nm, Fig. 13 c) that layered cirrus clouds or laminar cirrus are observed near the CPT
26 in these cold anomalies. Profiles of RHi observed from the Aura-MLS on 22 and 23 August 2017 co-located with
27 CALIOP show RHi values greater than 100 % at 100 hPa (~16.8 km) level, indicating supersaturation that resulted
28 in ice formation (see Fig. S10).
29

Formatted: Normal (Web), Left, Line spacing: single



1
2



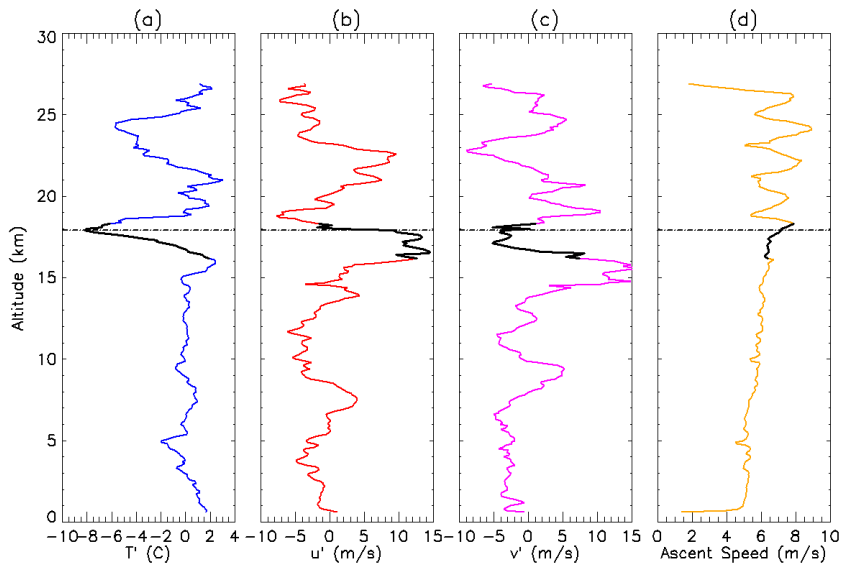
3

4 **Figure 13: (a) Map showing the locations of tropopause cirrus clouds (magenta filled circles) observed along**
 5 **the balloon trajectory (solid red line), CATS (dashed red line) and CALIOP (dashed blue lines) overpasses on**
 6 **22 and 23 August 2017. Vertical profile of backscattering ratio (shown by black line) obtained from (ba)**
 7 **COBALD data on 23 August 2017 at around 20:40 UTC over 17.45° N, 78.31° E, (cb) CALIOP on 23 August**
 8 **2017 at around 07:38 UTC over 16.99° N, 88.88° E, (cd) CATS on 23 August 2017 at around 00:59 UTC over**

1 ~~17.01° N, 92.68° E~~ and ~~(ed)~~ CALIOP on 22 August 2017 at around 19:07 UTC ~~over 16.99° N, 101.68° E.~~
 2 CALIOP and CATS profiles ~~intersecting with the back-trajectories~~ are averaged between 167° and 18° N.
 3 Blue line in ~~(bc)~~, ~~(de)~~ and ~~(ed)~~ represents the mean temperature profile obtained by averaging the
 4 corresponding ~~GMAO's GEOS-FPMERRA-2~~ temperature profiles provided with CALIOP and CATS data.
 5 Dashed ~~blue~~ red line shows the ~~nearest available co-incident and co-located~~ temperature profile obtained from
 6 ~~(ba)~~ radiosonde measurement ~~over location 1 (red plus symbol)~~, ~~(bc)~~ COSMIC GPS RO on 23 August 2017 at
 7 05:07 UTC ~~over location 2 (blue filled circle)~~ ~~over 20.13° N, 87.37° E~~, ~~(ed)~~ COSMIC GPS RO on 23 August
 8 2017 at 02:33 UTC over ~~location 3 (orange filled circle)~~ ~~18.29° N, 90.87° E~~, ~~(de)~~ COSMIC GPS RO on 22
 9 August 2017 at 23:42 UTC over ~~location 4 (olive filled circle)~~ ~~16.63° N, 100.04° E~~. ~~The H~~ horizontal red line in
 10 each panel marks the CPT.

Formatted: Font: 10 pt, Bold, Font color: Auto

12 The CPT temperature and CPT altitude over Hyderabad (within 400 km radius around TIFR-BF) on 23
 13 August 2017 exhibited a drastic change in the last 24 hours as observed from balloon and GNSS-RO observations as
 14 discussed earlier (in Table 32). Deep convective clouds that occurred over the land along the Indian East Coast in
 15 the late evening hours (as mentioned in Sect. 3.4.1) might also have helped in strengthening this tropopause cooling.
 16 CPT temperature was minimum and CPT altitude was maximum for this BATAL flight. All the IMD stations near



18 Figure 14: Vertical profile of (a) temperature anomaly, (b) zonal wind speed anomaly, (c) meridional wind
 19 speed anomaly and (d) ascent speed of the balloon observed on 23 August 2017. Anomalies are estimated by
 20 subtracting the monthly mean profile from the profile obtained on 23 August 2017. Mean profiles are
 21 obtained from all the radiosonde profiles at 00 UTC and BATAL flights over Hyderabad for August 2017.
 22 The black dashed horizontal line in each panel denotes the location of the CPT (at 17.9 km) observed on 23
 23 August 2017 at around 21:00 UTC from the balloon. Black shading in each profile shows the location of the
 24 tropopause cirrus cloud.

26 Hyderabad (Machilipatnam, Vizag, and Jagdalpur) recorded lower tropopause temperature on 24 August 2017 at 00
 27 UTC compared to that observed on 23 August 2017 at 00 UTC. The magnitude of tropopause cooling can be

1 expressed in terms of anomaly in the observed temperature with respect to the mean observed temperature over
2 Hyderabad. We construct a mean temperature profile over Hyderabad region during August 2017 using the
3 temperature profiles obtained from all (nine) the flights of BATAL-2017 campaign over TIFR-BF and daily 00 UTC
4 radiosonde data from Hyderabad airport. The vertical profile of the observed temperature anomaly for our balloon
5 flight on 23 August 2017 estimated after subtracting the mean temperature profile from it clearly shows a cold
6 anomaly of ~ -8 °C near the CPT region (Fig. 14 a) where CL5 was found. We also notice a wave-like pattern in the
7 temperature anomaly profile above 15 km altitude. Using the airborne data from the ATTREX campaign, Kim et al.
8 (2016) showed that about 86% of the cirrus clouds between 16.5 and 18 km over the Pacific are formed in the cold
9 anomalies induced by gravity waves. They also found that these clouds more often form in the negative slope of the
10 temperature anomaly, which is also true for CL5 (see the cloud shading in Fig. 14) but it is also present in the
11 positive anomaly above the tropopause as well up to the CL5 top altitude where ascent speed peaks and drops (see
12 Fig. 14d). Similar wave like pattern is also noticed in the anomaly profiles of zonal and meridional wind speed (Fig.
13 14b and 14c), estimated by subtracting the mean zonal and meridional speeds for August 2017 obtained from
14 BATAL flights and Hyderabad airport radiosonde data for August 2017. Such wave pattern is also reflected in the
15 spatial movement of the balloon as shown in Fig. S1. In addition to this, the ascent speed of the balloon also shows
16 oscillation above the CPT with its amplitude increasing with altitude (Fig. 14d). All these observations indicate
17 towards the possible influence of gravity waves in the tropopause cooling, which possibly led to ice formation after
18 reaching supersaturation with respect to ice. Recently, Martínez et al. (2021) have reported a case of extremely thin
19 cirrus cloud layer formed near the CPT over the Southwestern Indian Ocean using COBALD and CFH observations.
20 Using the spectral analysis (S-transform, Stockwell et al. (1996)) of temperature anomaly and ascent speed, they
21 suggested the role of homogeneous freezing under the influence of a high frequency gravity wave with a vertical
22 wavelength of 1.5 km. Using Hodograph analysis of radiosonde data following Leena et al. (2012), we estimated the
23 gravity wave characteristics. We found that the gravity wave was propagating from south-east direction to north-
24 west direction in the stratosphere (18-26 km) with a horizontal phase speed of about 18.8 m s^{-1} and a horizontal
25 wavelength of about 1770 km, confirming that it was generated from typhoon *Hato*.

26

27 **4 Summary**

28

29 In situ measurements in cirrus clouds with ice crystals smaller than $100 \mu\text{m}$ near the tropopause over the ASM
30 region are sparse, and the available observations mainly come from probes on aircraft that are traveling at rapid
31 speeds through the clouds, leading to shattering of ice crystals and failure to resolve small ice crystal habits. In this
32 paper, we have presented balloon-borne measurements of the optical and microphysical properties of a tropical
33 tropopause cirrus cloud layer obtained using a backscatter sonde and an optical particle counter on 23 August 2017
34 during the BATAL campaign over Hyderabad, India. This layer was a subvisible cirrus cloud located at an
35 extremely cold tropopause temperature of -86.4 °C. The top of this layer was found in the lower stratosphere at
36 about 18.3 km. Ice crystals in this cloud layer were smaller than $50 \mu\text{m}$ in diameter. Nearby lidar backscatter
37 measurements from the CATS onboard ISS confirmed the presence of this tropopause cirrus that extended more

1 than 500 km along the ISS orbit track. IWC for this layer was estimated independently from the backscatter
2 measurements and optical particle counter and found to be less than 0.2 mg m^{-3} . Simultaneous measurements of
3 backscatter coefficient from COBALD and extinction coefficient derived from Boulder Counter measurements
4 allowed us to derive a range-resolved lidar ratio for this tropopause cirrus cloud layer, whose average value is
5 $32.18 \pm 6.73 \text{ sr}$. We demonstrated that the combination of COBALD and Boulder Counter can be used to estimate
6 range-resolved lidar ratios for tropopause cirrus cloud layers, which may prove useful in validating lidar retrievals of
7 extinction coefficient. This estimate can be improved with higher ice particle sampling rate at more size channels
8 especially at smaller radii. We also investigated the formation mechanism of this layer using back-trajectories,
9 satellite, and ERA5 reanalysis data. Back-trajectories from the balloon measurement site and their intersection with
10 convective clouds observed in Himawari-8 brightness temperature images suggest that the layer was influenced by a
11 category-3 typhoon named *Hato*. Both Himawari-8 and CALIOP observations showed that *Hato* injected ice crystals
12 into the lower stratosphere causing a hydration patch as revealed by ERA5 WVMR and confirmed by the MLS
13 WVMR observations. These moist plumes were seen to be advected by the ASM anticyclonic flow towards
14 Hyderabad. Moreover, along the back-trajectories there were quasi-periodic cold and warm anomalies near the CPT
15 associated with updrafts and downdrafts, respectively. CATS and CALIOP observations showed the presence of
16 tropopause cirrus clouds in these cold anomalies. These perturbations are most likely caused by the gravity waves
17 induced by typhoon *Hato*. Signatures of such perturbations were also noticed in the temperature and wind profiles
18 obtained from our balloon observations. Through this case study, we conclude that the overshooting clouds in
19 typhoons can cause direct stratospheric hydration during the ASM in addition to the usual overshooting convective
20 systems. Following the ASM anticyclonic flow, this stratospheric hydration can get advected several thousands of
21 kilometres and subsequently may lead to tropopause cirrus clouds upon cooling induced by typhoon induced gravity
22 waves.

23 The occurrence frequency of tropopause-penetrating deep convective clouds (Aumann et al., 2018) and the
24 intensity of tropical cyclones are expected to increase in a warmer climate (Stocker et al., 2013; Emanuel, 2005),
25 which in turn are likely to increase the occurrence of ice-injections with consequences for the stratospheric
26 composition, thin tropopause cirrus clouds and further feedbacks on the global climate (Dessler et al., 2016;
27 Solomon et al., 2010). A recent modelling study (Smith et al., 2022) has found that the impact of convective
28 hydration in response to increased CO_2 depends not only on the frequency and penetration altitude of convective
29 overshooting into the stratosphere but also on large-scale temperatures in the TTL. In this context, the occurrence of
30 frequent deep convection and presence of cold temperatures in the TTL over the ASM anticyclone region are
31 important for convective hydration and tropopause cirrus cloud formation. In future, simultaneous measurements of
32 temperature, water vapour, and the microphysical properties of cirrus clouds using quasi-isentropic balloon flights
33 within the coldest regions of the ASM anticyclone will be planned to obtain a detailed understanding of the impacts
34 of overshooting convection on the formation of tropical tropopause cirrus clouds.
35

1 **Appendix A**

2 **A1 Data and Methods**

3
4 **Compact Optical Backscatter Aerosol Detector (COBALD)**

5 COBALD consists of two high power (500 mW) Light Emitting Diodes (LEDs) which emit light at 455 nm (blue) and 940 nm (near infrared) wavelengths. A silicon photodiode placed between the two LEDs collects the light backscattered from the air-borne particles (molecules, aerosols, and clouds). When connected with an iMet radiosonde, the instrument adds backscatter and monitor signals at both wavelengths to the radiosonde pressure, temperature, relative humidity, wind speed and wind direction data at a rate of 1 Hz to the receiving ground station. The concurrent profiles of pressure, temperature and backscattered counts are used to calculate backscatter ratio (BSR), the ratio of total (molecules and particulate) backscatter coefficient ($\beta = \beta_p + \beta_m$) to the molecular backscatter coefficient (β_m) at a given wavelength. The BSR is calibrated in a region of the atmosphere minimally affected by aerosols and adjusted with a reference density signal derived from pressure and temperature. The absolute error associated with BSR is within 5 % while its precision is better than 1 % in the UTLS region (Vernier et al., 2015).

15 ▲
16 **Lidar ratio**

17 The ratio of extinction to backscatter coefficient, often called the lidar ratio, is used in retrieving extinction coefficient from the backscatter measurements of elastic backscatter lidars. The retrieved extinction coefficient and hence the layer optical thickness are very sensitive to the magnitude of the lidar ratio used in the extinction retrieval, which depends on the number concentration, size and shape distributions and refractive index of the particles (Ackermann, 1998). Since microphysical properties of cirrus clouds mainly depend on temperature and RH_i (Heymsfield et al., 2017), it is essential to study the dependence of lidar ratio on these factors. The variation of lidar ratio within a cirrus cloud layer can be measured in situ or by using inelastic lidars, such as Raman lidars (Ansmann et al., 1992; Sakai et al., 2003) or high spectral resolution lidars (Grund and Eloranta, 1990). In case of elastic backscatter lidars, for an extinction coefficient retrieval the lidar ratio is usually assumed to be constant (range-independent) inside a cirrus cloud layer. Version 3 CATS lidar clouds products use a constant lidar ratio of 28 sr over land and 32 sr over the oceans for tropical ice clouds (CATS Data Release Notes Version 3.0, 2018). This approach of using a constant lidar ratio is unable to account for the natural variability of the actual lidar ratio leading to erroneous extinction coefficient and cloud optical thickness retrievals for cirrus clouds (Saito et al., 2017). Using multi-year nighttime CALIOP two-way transmission and collocated IIR absorption optical depth at 12.05 μm for single-layer semi-transparent cirrus cloud layers over the ocean, Garnier et al. (2015) derived temperature dependent multiple-scattering factor and a corresponding temperature-dependent parametrization of initial lidar ratio. Following this study, the multiple scattering factor and lidar ratio in CALIOP V4 algorithm are approximated by a sigmoid function of the centroid temperature of the 532 nm attenuated coefficient within the cloud layer (Young et al., 2018). According to this sigmoid function, the value of initial lidar ratio for a cirrus cloud layer with centroid temperature between -80 °C and -90 °C falls in the range of 20-22 sr. The introduction of this approach in the

Formatted: Font: 10 pt, Bold, Font color: Auto

Formatted: Font: Bold

Formatted: Font: 10 pt, Bold

Formatted: Font: Bold

Formatted: Justified, Line spacing: 1.5 lines

Formatted: Font: 10 pt

Formatted: Line spacing: 1.5 lines

Formatted: Font: 10 pt, Bold

1 CALIP V4 algorithm has resulted in the reduction of the relative uncertainty assigned to the initial lidar ratio for
2 semi-transparent ice clouds by 15 % compared to V3 algorithm (Young et al., 2018).

3 There are many studies on lidar ratio of cirrus clouds using lidars measurements (see Table 5 of Voudouri
4 et al. (2020)) but such studies using in situ measurements of subvisible cirrus clouds near the tropical tropopause are
5 rare. Our unique balloon measurements provided us independent in situ measurements of backscatter (from
6 COBALD) and extinction coefficients (from Boulder Counter) inside a subvisible cirrus layer near the CPT which
7 allowed us to estimate the vertical profile of lidar ratio as shown in Table 2.

Formatted: Indent: First line: 0.5"

Formatted: Left, Indent: First line: 0", Line spacing: single

10 **Data availability**

11 CALIPSO data were obtained from NASA Langley Research Centre Atmospheric Science Data Centre
12 (<https://asdc.larc.nasa.gov/project/CALIPSO>), GEOS-5 FP wind data from NASA GMAO and Himawari-8 data
13 from the University of Wisconsin - Madison Space Science and Engineering Centre (SSEC). Doppler weather radar
14 data were obtained from India Meteorological Department (IMD). Daily 00 UTC radiosonde data were obtained
15 from University of Wyoming (<https://weather.uwyo.edu/upperair/sounding.html>), GNSS-RO temperature profile
16 data from UCAR-COSMIC (<https://cdaac-www.cosmic.ucar.edu/>), ERA5 reanalysis data from Copernicus climate
17 data store (<https://cds.climate.copernicus.eu/cdsapp#!/dataset/reanalysis-era5-single-levels?tab=overview>), Aura-
18 MLS data from NASA-JPL (https://disc.gsfc.nasa.gov/datasets/ML2RHI_004/summary) and CATS data from
19 NASA-GSFC (<https://cats.gsfc.nasa.gov/>). BATAL data will be made available at <https://science->
20 [data.larc.nasa.gov/BATAL/data.html](https://science-data.larc.nasa.gov/BATAL/data.html) and can also be obtained through request.

22 **Author contribution**

23 AKP wrote the manuscript draft. JPV, TDF, BSK, HG, MVR, AKP and AJ organized the field campaign. AKP and
24 JPV collected in situ data. TDF and HG provided back trajectories. AKP and JPV analysed in situ and back-
25 trajectory data. KMB provided cloud top heights from Himawari-8 along the back-trajectories. MAA contributed to
26 CALIPSO data analysis. AKP analysed CATS, CALIPSO, MLS, GNSS-RO and ERA5 data. FGW provided
27 calibrated COBALD data. SD contributed to ERA5 data analysis. KAJ provided doppler weather radar analysis.
28 MVR provided gravity wave characteristics. All the authors reviewed and edited the manuscript.

30 **Competing interests**

31 The authors declare that they have no conflict of interest.

33 **Acknowledgements**

34 This paper is dedicated to our great colleagues Mr. B. Suneel Kumar and Dr. T. Duncan Fairlie who made
35 significant contributions to the BATAL project and left us much too early. This work was carried out under ISRO-
36 NASA joint project called BATAL. The 2017 balloon deployment and the analysis of the data were supported by the
37 NASA ROSES Upper Atmospheric Research and the Upper Atmospheric Composition Observations programs
38 through an IDIQ task at NASA Langley Research Centre. AKP is thankful to the Physical Research Laboratory in

1 Ahmedabad, India for supporting his participation in the BATAL-2017 field campaign. He is also thankful for the
2 support provided by the NASA Postdoctoral Program (NPP) fellowship administered by Universities Space
3 Research Association, NASA Langley Research Centre, and National Institute of Aerospace in conducting this
4 research. We thank the engineers, technicians, and staffs at TIFR Balloon Facility in Hyderabad and National
5 Atmospheric Research Laboratory at Gadanki, India for their valuable contributions towards the scientific, technical,
6 and logistical support provided during the BATAL campaign. We also thank Mijeong Park from NCAR for helpful
7 discussion.

1 **References**

2
3 Ackermann, J.: The Extinction-to-Backscatter Ratio of Tropospheric Aerosol: A Numerical Study, Journal of Atmospheric and Oceanic Technology, 15, 1043–1050, [https://doi.org/10.1175/1520-0426\(1998\)015<1043:TETBRO>2.0.CO;2](https://doi.org/10.1175/1520-0426(1998)015<1043:TETBRO>2.0.CO;2), 1998.
4
5
6
7 Ansmann, A., Wandinger, U., Riebesell, M., Weitkamp, C., and Michaelis, W.: Independent measurement of extinction and backscatter profiles in cirrus clouds by using a combined Raman elastic-backscatter lidar, Appl. Opt., AO, 31, 7113–7131, <https://doi.org/10.1364/AO.31.007113>, 1992.
8
9
10
11 Anthes, R. A., Bernhardt, P. A., Chen, Y., Cucurull, L., Dymond, K. F., Ector, D., Healy, S. B., Ho, S.-P., Hunt, D. C., Kuo, Y.-H., Liu, H., Manning, K., McCormick, C., Meehan, T. K., Randel, W. J., Rocken, C., Schreiner, W. S., Sokolovskiy, S. V., Syndergaard, S., Thompson, D. C., Trenberth, K. E., Wee, T.-K., Yen, N. L., and Zeng, Z.: The COSMIC/FORMOSAT-3 Mission: Early Results, Bulletin of the American Meteorological Society, 89, 313–334, <https://doi.org/10.1175/BAMS-89-3-313>, 2008.
12
13
14
15
16 Aumann, H. H., Behrangi, A., and Wang, Y.: Increased Frequency of Extreme Tropical Deep Convection: AIRS Observations and Climate Model Predictions, Geophysical Research Letters, 45, 13,530-13,537, <https://doi.org/10.1029/2018GL079423>, 2018.
17
18
19
20
21 Baumgardner, D., Abel, S. J., Axisa, D., Cotton, R., Crosier, J., Field, P., Gurganus, C., Heymsfield, A., Korolev, A., Krämer, M., Lawson, P., McFarquhar, G., Ulanowski, Z., and Um, J.: Cloud Ice Properties: In Situ Measurement Challenges, Meteorological Monographs, 58, 9.1-9.23, <https://doi.org/10.1175/AMSMONOGRAPHS-D-16-0011.1>, 2017.
22
23
24
25
26 Bedka, K. M. and Khlopenkov, K.: A Probabilistic Multispectral Pattern Recognition Method for Detection of Overshooting Cloud Tops Using Passive Satellite Imager Observations, Journal of Applied Meteorology and Climatology, 55, 1983–2005, <https://doi.org/10.1175/JAMC-D-15-0249.1>, 2016.
27
28
29
30 Bessho, K., Date, K., Hayashi, M., Ikeda, A., Imai, T., Inoue, H., Kumagai, Y., Miyakawa, T., Murata, H., Ohno, T., Okuyama, A., Oyama, R., Sasaki, Y., Shimazu, Y., Shimoji, K., Sumida, Y., Suzuki, M., Taniguchi, H., Tsuchiyama, H., Uesawa, D., Yokota, H., and Yoshida, R.: An Introduction to Himawari-8/9— Japan’s New-Generation Geostationary Meteorological Satellites, Journal of the Meteorological Society of Japan. Ser. II, 94, 151–183, <https://doi.org/10.2151/jmsj.2016-009>, 2016.
31
32
33
34
35
36 Biondi, R., Ho, S.-P., Randel, W., Syndergaard, S., and Neubert, T.: Tropical cyclone cloud-top height and vertical temperature structure detection using GPS radio occultation measurements, Journal of Geophysical Research: Atmospheres, 118, 5247–5259, <https://doi.org/10.1002/jgrd.50448>, 2013.
37
38
39
40 Biondi, R., Steiner, A. K., Kirchengast, G., and Rieckh, T.: Characterization of thermal structure and conditions for overshooting of tropical and extratropical cyclones with GPS radio occultation, Atmospheric Chemistry and Physics, 15, 5181–5193, <https://doi.org/10.5194/acp-15-5181-2015>, 2015.
41
42
43
44 Biondi, R., Steiner, A. K., Kirchengast, G., Brenot, H., and Rieckh, T.: Supporting the detection and monitoring of volcanic clouds: A promising new application of Global Navigation Satellite System radio occultation, Advances in Space Research, 60, 2707–2722, <https://doi.org/10.1016/j.asr.2017.06.039>, 2017.
45
46
47
48 Bourgeois, Q., Ekman, A. M. L., Igel, M. R., and Krejci, R.: Ubiquity and impact of thin mid-level clouds in the tropics, Nat Commun, 7, 12432, <https://doi.org/10.1038/ncomms12432>, 2016.
49
50
51 Brabec, M., Wienhold, F. G., Luo, B. P., Vömel, H., Immler, F., Steiner, P., Hausammann, E., Weers, U., and Peter, T.: Particle backscatter and relative humidity measured across cirrus clouds and comparison with microphysical cirrus modelling, Atmospheric Chemistry and Physics, 12, 9135–9148, <https://doi.org/10.5194/acp-12-9135-2012>, 2012.
52
53
54

Formatted: Font: 10 pt

Formatted: Normal

Formatted: Font: 10 pt

Formatted: Justified

1 Garnier, A., Pelon, J., Vaughan, M. A., Winker, D. M., Trepte, C. R., and Dubuisson, P.: Lidar multiple scattering
2 factors inferred from CALIPSO lidar and IIR retrievals of semi-transparent cirrus cloud optical depths over oceans,
3 Atmos. Meas. Tech., 8, 2759–2774, <https://doi.org/10.5194/amt-8-2759-2015>, 2015.

4

5 Gasparini, B. and Lohmann, U.: Why cirrus cloud seeding cannot substantially cool the planet, Journal of
6 Geophysical Research: Atmospheres, 121, 4877–4893, <https://doi.org/10.1002/2015JD024666>, 2016.

7

8 Grund, C. J. and Eloranta, E. W.: The 27–28 October 1986 FIRE IFO Cirrus Case Study: Cloud Optical Properties
9 Determined by High Spectral Resolution Lidar, Monthly Weather Review, 118, 2344–2355,
10 [https://doi.org/10.1175/1520-0493\(1990\)118<2344:TOFICC>2.0.CO;2](https://doi.org/10.1175/1520-0493(1990)118<2344:TOFICC>2.0.CO;2), 1990.

11

12 He, Q., Ma, J., Zheng, X., Yan, X., Vömel, H., Wienhold, F. G., Gao, W., Liu, D., Shi, G., and Cheng, T.:
13 Observational evidence of particle hygroscopic growth in the upper troposphere–lower stratosphere (UTLS) over the
14 Tibetan Plateau, Atmos. Chem. Phys., 19, 8399–8406, <https://doi.org/10.5194/acp-19-8399-2019>, 2019.

15

16 He, Q. S., Li, C. C., Ma, J. Z., Wang, H. Q., Shi, G. M., Liang, Z. R., Luan, Q., Geng, F. H., and Zhou, X. W.: The
17 Properties and Formation of Cirrus Clouds over the Tibetan Plateau Based on Summertime Lidar Measurements,
18 Journal of the Atmospheric Sciences, 70, 901–915, <https://doi.org/10.1175/JAS-D-12-0171.1>, 2013.

19

20 Hersbach, H., Bell, B., Berrisford, P., Hirahara, S., Horányi, A., Muñoz-Sabater, J., Nicolas, J., Peubey, C., Radu,
21 R., Schepers, D., Simmons, A., Soci, C., Abdalla, S., Abellan, X., Balsamo, G., Bechtold, P., Biavati, G., Bidlot, J.,
22 Bonavita, M., De Chiara, G., Dahlgren, P., Dee, D., Diamantakis, M., Dragani, R., Flemming, J., Forbes, R.,
23 Fuentes, M., Geer, A., Haimberger, L., Healy, S., Hogan, R. J., Hólm, E., Janisková, M., Keeley, S., Laloyaux, P.,
24 Lopez, P., Lupu, C., Radnoti, G., de Rosnay, P., Rozum, I., Vamborg, F., Villaume, S., and Thépaut, J.-N.: The
25 ERA5 global reanalysis, Quarterly Journal of the Royal Meteorological Society, 146, 1999–2049,
26 <https://doi.org/10.1002/qj.3803>, 2020.

27

28 Heymsfield, A., Winker, D., Avery, M., Vaughan, M., Diskin, G., Deng, M., Mitev, V., and Matthey, R.:
29 Relationships between Ice Water Content and Volume Extinction Coefficient from In Situ Observations for
30 Temperatures from 0° to –86°C: Implications for Spaceborne Lidar Retrievals, Journal of Applied Meteorology and
31 Climatology, 53, 479–505, <https://doi.org/10.1175/JAMC-D-13-087.1>, 2014.

32

33 Heymsfield, A. J. and Westbrook, C. D.: Advances in the Estimation of Ice Particle Fall Speeds Using Laboratory
34 and Field Measurements, Journal of the Atmospheric Sciences, 67, 2469–2482,
35 <https://doi.org/10.1175/2010JAS3379.1>, 2010.

36

37 Heymsfield, A. J., Krämer, M., Luebke, A., Brown, P., Cziczo, D. J., Franklin, C., Lawson, P., Lohmann, U.,
38 McFarquhar, G., Ulanowski, Z., and Tricht, K. V.: Cirrus Clouds, Meteorological Monographs, 58, 2.1–2.26,
39 <https://doi.org/10.1175/AMSMONOGRAPH5-D-16-0010.1>, 2017.

40

41 Hong, Y., Liu, G., and Li, J.-L. F.: Assessing the Radiative Effects of Global Ice Clouds Based on CloudSat and
42 CALIPSO Measurements, Journal of Climate, 29, 7651–7674, <https://doi.org/10.1175/JCLI-D-15-0799.1>, 2016.

43

44 Höpfner, M., Ungerer, J., Borrmann, S., Wagner, R., Spang, R., Riese, M., Stiller, G., Appel, O., Batenburg, A.
45 M., Bucci, S., Cairo, F., Dragoneas, A., Friedl-Vallon, F., Hünig, A., Johansson, S., Krasauskas, L., Legras, B.,
46 Leisner, T., Mahnke, C., Möhler, O., Molleker, S., Müller, R., Neubert, T., Orphal, J., Preusse, P., Rex, M.,
47 Saathoff, H., Stroh, F., Weigel, R., and Wohltmann, I.: Ammonium nitrate particles formed in upper troposphere
48 from ground ammonia sources during Asian monsoons, Nat. Geosci., 12, 608–612, [https://doi.org/10.1038/s41561-](https://doi.org/10.1038/s41561-019-0385-8)
49 019-0385-8, 2019.

50

51 Horinouchi, T., Shimada, U., and Wada, A.: Convective Bursts With Gravity Waves in Tropical Cyclones: Case
52 Study With the Himawari-8 Satellite and Idealized Numerical Study, Geophysical Research Letters, 47,
53 e2019GL086295, <https://doi.org/10.1029/2019GL086295>, 2020.

Formatted: Font: 10 pt

Formatted: Normal

Formatted: Font: 10 pt

1
2 Jensen, E. J., Toon, O. B., Pfister, L., and Selkirk, H. B.: Dehydration of the upper troposphere and lower
3 stratosphere by subvisible cirrus clouds near the tropical tropopause, *Geophysical Research Letters*, 23, 825–828,
4 <https://doi.org/10.1029/96GL00722>, 1996.

5
6 Jensen, E. J., Pfister, L., Jordan, D. E., Bui, T. V., Ueyama, R., Singh, H. B., Thornberry, T. D., Rollins, A. W., Gao,
7 R.-S., Fahey, D. W., Rosenlof, K. H., Elkins, J. W., Diskin, G. S., DiGangi, J. P., Lawson, R. P., Woods, S., Atlas,
8 E. L., Rodriguez, M. A. N., Wofsy, S. C., Pittman, J., Bardeen, C. G., Toon, O. B., Kindel, B. C., Newman, P. A.,
9 McGill, M. J., Hlavka, D. L., Lait, L. R., Schoeberl, M. R., Bergman, J. W., Selkirk, H. B., Alexander, M. J., Kim,
10 J.-E., Lim, B. H., Stutz, J., and Pfeilsticker, K.: The NASA Airborne Tropical Tropopause Experiment: High-
11 Altitude Aircraft Measurements in the Tropical Western Pacific, *Bulletin of the American Meteorological Society*,
12 98, 129–143, <https://doi.org/10.1175/BAMS-D-14-00263.1>, 2017.

13
14 Jensen, E. J., Pan, L. L., Honomichl, S., Diskin, G. S., Krämer, M., Spelten, N., Günther, G., Hurst, D. F., Fujiwara,
15 M., Vömel, H., Selkirk, H. B., Suzuki, J., Schwartz, M. J., and Smith, J. B.: Assessment of Observational Evidence
16 for Direct Convective Hydration of the Lower Stratosphere, *Journal of Geophysical Research: Atmospheres*, 125,
17 e2020JD032793, <https://doi.org/10.1029/2020JD032793>, 2020.

18
19 Jiang, B., Lin, W., Hu, C., and Wu, Y.: Tropical cyclones impact on tropopause and the lower stratosphere vapour
20 based on satellite data, *Atmospheric Science Letters*, 21, e1006, <https://doi.org/10.1002/asl.1006>, 2020.

21
22 Kärcher, B.: Cirrus Clouds and Their Response to Anthropogenic Activities, *Curr Clim Change Rep*, 3, 45–57,
23 <https://doi.org/10.1007/s40641-017-0060-3>, 2017.

24
25 Khaykin, S., Lukyanov, A., and Williams, E.: Hydration of the lower stratosphere by ice crystal geysers over land
26 convective systems, *Atmos. Chem. Phys.*, 13, 2009.

27
28 Khaykin, S., Legras, B., Bucci, S., Sellitto, P., Isaksen, L., Tencé, F., Bekki, S., Bourassa, A., Rieger, L., Zawada,
29 D., Jumelet, J., and Godin-Beekmann, S.: The 2019/20 Australian wildfires generated a persistent smoke-charged
30 vortex rising up to 35 km altitude, *Commun Earth Environ*, 1, 1–12, <https://doi.org/10.1038/s43247-020-00022-5>,
31 2020.

32
33 Khaykin, S., Moyer, E., Krämer, M., Clouser, B., Bucci, S., Legras, B., Lykov, A., Afchine, A., Cairo, F.,
34 Formanyuk, I., Mitev, V., Matthey, R., Rolf, C., Singer, C., Spelten, N., Volkov, V., Yushkov, V., and Stroth, F.:
35 Persistence of moist plumes from overshooting convection in the Asian monsoon anticyclone, *Gases/Field*
36 *Measurements/Stratosphere/Physics* (physical properties and processes), <https://doi.org/10.5194/acp-2021-653>,
37 2021.

38
39 Khaykin, S. M., Moyer, E., Krämer, M., Clouser, B., Bucci, S., Legras, B., Lykov, A., Afchine, A., Cairo, F.,
40 Formanyuk, I., Mitev, V., Matthey, R., Rolf, C., Singer, C. E., Spelten, N., Volkov, V., Yushkov, V., and Stroth, F.:
41 Persistence of moist plumes from overshooting convection in the Asian monsoon anticyclone, *Atmospheric*
42 *Chemistry and Physics*, 22, 3169–3189, <https://doi.org/10.5194/acp-22-3169-2022>, 2022.

43
44 Khlopenkov, K. V., Bedka, K. M., Cooney, J. W., and Iterly, K.: Recent Advances in Detection of Overshooting
45 Cloud Tops From Longwave Infrared Satellite Imagery, *Journal of Geophysical Research: Atmospheres*, 126,
46 e2020JD034359, <https://doi.org/10.1029/2020JD034359>, 2021.

47
48 Kim, J., Randel, W. J., and Birner, T.: Convectively Driven Tropopause-Level Cooling and Its Influences on
49 Stratospheric Moisture, *Journal of Geophysical Research: Atmospheres*, 123, 590–606,
50 <https://doi.org/10.1002/2017JD027080>, 2018.

51
52 Kim, J.-E. and Alexander, M. J.: Direct impacts of waves on tropical cold point tropopause temperature,
53 *Geophysical Research Letters*, 42, 1584–1592, <https://doi.org/10.1002/2014GL062737>, 2015.

Formatted: Normal

Formatted: Font: 10 pt

1 Liou, Y. A., Pavelyev, A. G., Huang, C. Y., Igarashi, K., Hocke, K., and Yan, S. K.: Analytic method for
2 observation of the gravity waves using radio occultation data, *Geophysical Research Letters*, 30,
3 <https://doi.org/10.1029/2003GL017818>, 2003.

4 Lohmann, U. and Gasparini, B.: A cirrus cloud climate dial?, *Science*, 357, 248–249,
5 <https://doi.org/10.1126/science.aan3325>, 2017.

6 Martins, E., Noel, V., and Chepfer, H.: Properties of cirrus and subvisible cirrus from nighttime Cloud-Aerosol
7 Lidar with Orthogonal Polarization (CALIOP), related to atmospheric dynamics and water vapor, *Journal of
8 Geophysical Research: Atmospheres*, 116, <https://doi.org/10.1029/2010JD014519>, 2011.

9 Mitchell, D. L., Rasch, P., Ivanova, D., McFarquhar, G., and Nousiainen, T.: Impact of small ice crystal assumptions
10 on ice sedimentation rates in cirrus clouds and GCM simulations, *Geophysical Research Letters*, 35,
11 <https://doi.org/10.1029/2008GL033552>, 2008.

12 Murphy, D. M. and Koop, T.: Review of the vapour pressures of ice and supercooled water for atmospheric
13 applications, *Quarterly Journal of the Royal Meteorological Society*, 131, 1539–1565,
14 <https://doi.org/10.1256/qj.04.94>, 2005.

15 Nolan, D. S. and Zhang, J. A.: Spiral gravity waves radiating from tropical cyclones, *Geophysical Research Letters*,
16 44, 3924–3931, <https://doi.org/10.1002/2017GL073572>, 2017.

17 Nützel, M., Podglajen, A., Garny, H., and Ploeger, F.: Quantification of water vapour transport from the Asian
18 monsoon to the stratosphere, *Atmospheric Chemistry and Physics*, 19, 8947–8966, <https://doi.org/10.5194/acp-19-8947-2019>, 2019.

19 Pandit, A. K., Gadhavi, H. S., Venkat Ratnam, M., Raghunath, K., Rao, S. V. B., and Jayaraman, A.: Long-term
20 trend analysis and climatology of tropical cirrus clouds using 16 years of lidar data set over Southern India,
21 *Atmospheric Chemistry and Physics*, 15, 13833–13848, <https://doi.org/10.5194/acp-15-13833-2015>, 2015.

22 Podglajen, A., Plougonven, R., Hertzog, A., and Jensen, E.: Impact of gravity waves on the motion and distribution
23 of atmospheric ice particles, *Atmospheric Chemistry and Physics*, 18, 10799–10823, <https://doi.org/10.5194/acp-18-10799-2018>, 2018.

24 Pun, I.-F., Chan, J. C. L., Lin, I.-I., Chan, K. T. F., Price, J. F., Ko, D. S., Lien, C.-C., Wu, Y.-L., and Huang, H.-C.:
25 Rapid Intensification of Typhoon Hato (2017) over Shallow Water, *Sustainability*, 11, 3709,
26 <https://doi.org/10.3390/su11133709>, 2019.

27 Randel, W. J. and Jensen, E. J.: Physical processes in the tropical tropopause layer and their roles in a changing
28 climate, *Nature Geosci*, 6, 169–176, <https://doi.org/10.1038/ngeo1733>, 2013.

29 Ravindra Babu, S., Venkat Ratnam, M., Basha, G., Krishnamurthy, B. V., and Venkateswararao, B.: Effect of
30 tropical cyclones on the tropical tropopause parameters observed using COSMIC GPS RO data, *Atmospheric
31 Chemistry and Physics*, 15, 10239–10249, <https://doi.org/10.5194/acp-15-10239-2015>, 2015.

32 Ravindrababu, S., Ratnam, M. V., Basha, G., Liou, Y.-A., and Reddy, N. N.: Large Anomalies in the Tropical Upper
33 Troposphere Lower Stratosphere (UTLS) Trace Gases Observed during the Extreme 2015–16 El Niño Event by
34 Using Satellite Measurements, Remote Sensing, 11, 687, <https://doi.org/10.3390/rs11060687>, 2019.

35 Reinares Martínez, I., Evan, S., Wienhold, F. G., Brioude, J., Jensen, E. J., Thornberry, T. D., Héron, D., Verreyken,
36 B., Körner, S., Vömel, H., Metzger, J.-M., and Posny, F.: Unprecedented Observations of a Nascent In Situ Cirrus in
37 the Tropical Tropopause Layer, *Geophysical Research Letters*, 48, e2020GL090936,
38 <https://doi.org/10.1029/2020GL090936>, 2021.

Formatted: Normal

Formatted: Font: 10 pt

1
2 Rollins, A. W., Thornberry, T. D., Gao, R. S., Woods, S., Lawson, R. P., Bui, T. P., Jensen, E. J., and Fahey, D. W.:
3 Observational constraints on the efficiency of dehydration mechanisms in the tropical tropopause layer, *Geophysical*
4 *Research Letters*, 43, 2912–2918, <https://doi.org/10.1002/2016GL067972>, 2016.

5
6 Romps, D. M. and Kuang, Z.: Overshooting convection in tropical cyclones, *Geophysical Research Letters*, 36,
7 <https://doi.org/10.1029/2009GL037396>, 2009.

8
9 Saito, M., Iwabuchi, H., Yang, P., Tang, G., King, M. D., and Sekiguchi, M.: Ice particle morphology and
10 microphysical properties of cirrus clouds inferred from combined CALIOP-IIR measurements, *Journal of*
11 *Geophysical Research: Atmospheres*, 122, 4440–4462, <https://doi.org/10.1002/2016JD026080>, 2017.

12
13 Sakai, T., Nagai, T., Nakazato, M., Mano, Y., and Matsumura, T.: Ice clouds and Asian dust studied with lidar
14 measurements of particle extinction-to-backscatter ratio, particle depolarization, and water-vapor mixing ratio over
15 Tsukuba, *Appl. Opt.*, AO, 42, 7103–7116, <https://doi.org/10.1364/AO.42.007103>, 2003.

16
17 Sanderson, B. M., Piani, C., Ingram, W. J., Stone, D. A., and Allen, M. R.: Towards constraining climate sensitivity
18 by linear analysis of feedback patterns in thousands of perturbed-physics GCM simulations, *Clim Dyn*, 30, 175–190,
19 <https://doi.org/10.1007/s00382-007-0280-7>, 2008.

20
21 Schoeberl, M., Dessler, A., Ye, H., Wang, T., Avery, M., and Jensen, E.: The impact of gravity waves and cloud
22 nucleation threshold on stratospheric water and tropical tropospheric cloud fraction, *Earth and Space Science*, 3,
23 295–305, <https://doi.org/10.1002/2016EA000180>, 2016.

24
25 Schoeberl, M. R., Jensen, E. J., and Woods, S.: Gravity waves amplify upper tropospheric dehydration by clouds,
26 *Earth and Space Science*, 2, 485–500, <https://doi.org/10.1002/2015EA000127>, 2015.

27
28 Schoeberl, M. R., Jensen, E. J., Pfister, L., Ueyama, R., Wang, T., Selkirk, H., Avery, M., Thornberry, T., and
29 Dessler, A. E.: Water Vapor, Clouds, and Saturation in the Tropical Tropopause Layer, *Journal of Geophysical*
30 *Research: Atmospheres*, 124, 3984–4003, <https://doi.org/10.1029/2018JD029849>, 2019.

31
32 Shibata, T., Vömel, H., Hamdi, S., Kaloka, S., Hasebe, F., Fujiwara, M., and Shiotani, M.: Tropical cirrus clouds
33 near cold point tropopause under ice supersaturated conditions observed by lidar and balloon-borne cryogenic frost
34 point hygrometer, *Journal of Geophysical Research: Atmospheres*, 112, <https://doi.org/10.1029/2006JD007361>,
35 2007.

36
37 Shibata, T., Hayashi, M., Naganuma, A., Hara, N., Hara, K., Hasebe, F., Shimizu, K., Komala, N., Inai, Y., Vömel,
38 H., Hamdi, S., Iwasaki, S., Fujiwara, M., Shiotani, M., Ogino, S.-Y., and Nishi, N.: Cirrus cloud appearance in a
39 volcanic aerosol layer around the tropical cold point tropopause over Biak, Indonesia, in January 2011, *Journal of*
40 *Geophysical Research: Atmospheres*, 117, <https://doi.org/10.1029/2011JD017029>, 2012.

41
42 Smith, J. B., Wilmouth, D. M., Bedka, K. M., Bowman, K. P., Homeyer, C. R., Dykema, J. A., Sargent, M. R.,
43 Clapp, C. E., Leroy, S. S., Sayres, D. S., Dean-Day, J. M., Bui, T. P., and Anderson, J. G.: A case study of
44 convectively sourced water vapor observed in the overworld stratosphere over the United States, *Journal of*
45 *Geophysical Research: Atmospheres*, 122, 9529–9554, <https://doi.org/10.1002/2017JD026831>, 2017.

46
47 Smith, J. W., Bushell, A. C., Butchart, N., Haynes, P. H., and Maycock, A. C.: The Effect of Convective Injection of
48 Ice on Stratospheric Water Vapor in a Changing Climate, *Geophysical Research Letters*, 49, e2021GL097386,
49 <https://doi.org/10.1029/2021GL097386>, 2022.

50
51 Solomon, S., Rosenlof, K. H., Portmann, R. W., Daniel, J. S., Davis, S. M., Sanford, T. J., and Plattner, G.-K.:
52 Contributions of Stratospheric Water Vapor to Decadal Changes in the Rate of Global Warming, *Science*, 327,
53 1219–1223, <https://doi.org/10.1126/science.1182488>, 2010.

Formatted: Normal

Formatted: Font: 10 pt

1 Wang, X., Dessler, A. E., Schoeberl, M. R., Yu, W., and Wang, T.: Impact of convectively lofted ice on the seasonal
 2 cycle of water vapor in the tropical tropopause layer, *Atmospheric Chemistry and Physics*, 19, 14621–14636,
 3 <https://doi.org/10.5194/acp-19-14621-2019>, 2019.

4

5 Winker, D. M., Vaughan, M. A., Omar, A., Hu, Y., Powell, K. A., Liu, Z., Hunt, W. H., and Young, S. A.:
 6 Overview of the CALIPSO Mission and CALIOP Data Processing Algorithms, *Journal of Atmospheric and Oceanic*
 7 *Technology*, 26, 2310–2323, <https://doi.org/10.1175/2009JTECHA1281.1>, 2009.

8

9 Wolf, V., Kuhn, T., Milz, M., Voelger, P., Krämer, M., and Rolf, C.: Arctic ice clouds over northern Sweden:
 10 microphysical properties studied with the Balloon-borne Ice Cloud particle Imager B-ICI, *Atmospheric Chemistry*
 11 *and Physics*, 18, 17371–17386, <https://doi.org/10.5194/acp-18-17371-2018>, 2018.

12

13 Woods, S., Lawson, R. P., Jensen, E., Bui, T. P., Thornberry, T., Rollins, A., Pfister, L., and Avery, M.:
 14 Microphysical Properties of Tropical Tropopause Layer Cirrus, *Journal of Geophysical Research: Atmospheres*,
 15 123, 6053–6069, <https://doi.org/10.1029/2017JD028068>, 2018.

16

17 Wu, J. F., Xue, X. H., Hoffmann, L., Dou, X. K., Li, H. M., and Chen, T. D.: A case study of typhoon-induced
 18 gravity waves and the orographic impacts related to Typhoon Mindulle (2004) over Taiwan, *Journal of Geophysical*
 19 *Research: Atmospheres*, 120, 9193–9207, <https://doi.org/10.1002/2015JD023517>, 2015.

20

21 Yorks, J. E., McGill, M. J., Scott, V. S., Wake, S. W., Kupchock, A., Hlavka, D. L., Hart, W. D., and Selmer, P. A.:
 22 The Airborne Cloud–Aerosol Transport System: Overview and Description of the Instrument and Retrieval
 23 Algorithms, *Journal of Atmospheric and Oceanic Technology*, 31, 2482–2497, <https://doi.org/10.1175/JTECH-D-14-00044.1>, 2014.

24

25

26 Young, S. A., Vaughan, M. A., Garnier, A., Tackett, J. L., Lambeth, J. D., and Powell, K. A.: Extinction and optical
 27 depth retrievals for CALIPSO’s Version 4 data release, *Atmospheric Measurement Techniques*, 11, 5701–5727,
 28 <https://doi.org/10.5194/amt-11-5701-2018>, 2018.

29

Formatted: Font: 10 pt

Formatted: Normal

Formatted: Font: 10 pt

Formatted: Justified